

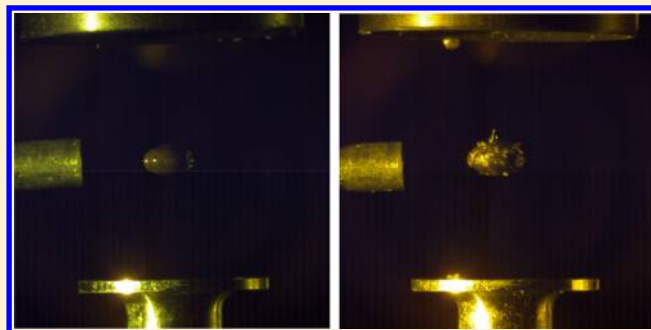
Spectroscopic Study on the Intermediates and Reaction Rates in the Oxidation of Levitated Droplets of Energetic Ionic Liquids by Nitrogen Dioxide

Stephen J. Brotton,[†] Michael Lucas,[†] Tonya N. Jensen,[‡] Scott L. Anderson,[‡] and Ralf I. Kaiser^{*,†}

[†]Department of Chemistry, University of Hawaii at Manoa, Honolulu, Hawaii 96822, United States

[‡]Department of Chemistry, University of Utah, Salt Lake City, Utah 84112, United States

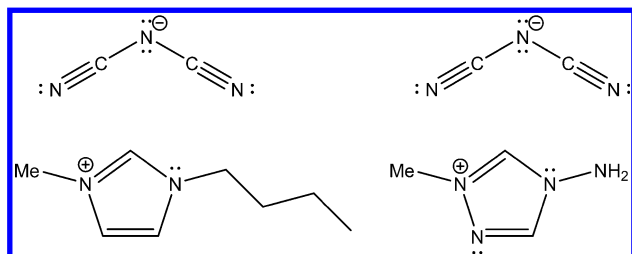
ABSTRACT: To optimize the performance of hypergolic, ionic-liquid-based fuels, it is critical to understand the fundamental reaction mechanisms of ionic liquids (ILs) with the oxidizers. We consequently explored the reactions between a single levitated droplet of 1-butyl-3-methylimidazolium dicyanamide ([BMIM][DCA]), with and without hydrogen-capped boron nanoparticles, and the oxidizer nitrogen dioxide (NO₂). The apparatus consists of an ultrasonic levitator enclosed within a pressure-compatible process chamber interfaced to complementary Fourier-transform infrared (FTIR), Raman, and ultraviolet–visible spectroscopic probes. First, the vibrational modes for the Raman and FTIR spectra of unreacted [BMIM][DCA] are assigned. We subsequently investigated the new structure in the infrared and Raman spectra produced by the reaction of the IL with the oxidizer. The newly produced peaks are consistent with the formation of the functional groups of organic nitro-compounds including the organic nitrites (RONO), nitroamines (RR'NNO₂), aromatic nitro-compounds (ArNO₂), and carbonitrates (RR'C=NO₂⁻), which suggests that the nitrogen or oxygen atom of the nitrogen dioxide reactant bonds to a carbon or nitrogen atom of [BMIM][DCA]. Comparison of the rate constants for the oxidation of pure and boron-doped [BMIM][DCA] at 300 K shows that the boron-doping reduces the reaction rate by a factor of approximately 2. These results are compared to the oxidation processes of 1-methyl-4-amino-1,2,4-triazolium dicyanamide ([MAT][DCA]) with nitrogen dioxide (NO₂) studied previously in our laboratory revealing that [BMIM][DCA] oxidizes faster than [MAT][DCA] by a factor of about 20. The present measurements are the first studies on the reaction rates for the oxidation of levitated ionic-liquid droplets.



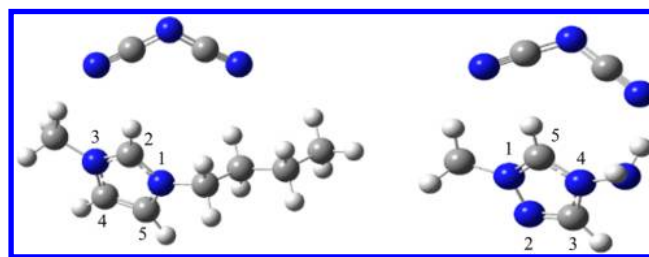
1. INTRODUCTION

A room-temperature ionic liquid (RTIL) is defined as a substance composed of ions that is liquid at room temperature (293 K).¹ Whereas conventional liquids like water (H₂O)

Scheme 1. (Left) Structure of [BMIM][DCA] Showing the [DCA]⁻ Anion and the Positions of the Methyl (–CH₃) and Butyl (–C₄H₉) Functional Groups on the Imidazolium Ring (C₃N₂H₃); (Right) Structure of [MAT][DCA] Showing the [DCA]⁻ Anion and the Locations of the Methyl (–CH₃) and Amino (–NH₂) Functional Groups on the Triazolium Ring (C₂N₃H₂)



Scheme 2. Optimized Structures of [BMIM][DCA] (Left) and [MAT][DCA] (Right) Displaying the Numbering Convention for the Positions of the Atoms in the Imidazolium or Triazolium Ring, Respectively^a



^aFor the [BMIM][DCA], the locations of the three ring protons H2, H4, and H5 are shown.

Received: May 31, 2018

Revised: August 3, 2018

Published: August 3, 2018

primarily consist of electrically neutral molecules, ionic liquids are constituted of ions and short-lived ion pairs.^{1–3} Also named as a “salt in the liquid state”, RTILs possess unique properties such as low vapor pressures, ionic conductivities, high-temperature stabilities of up to 718 K for 1-ethyl-3-methylimidazolium tetrafluoroborate ([EMIM][BF₄]), and the ability to dissolve a wide range of substances including carbon dioxide (CO₂) or aldehydes.⁴ Consequently, RTILs have received considerable interest in the past decade from the green chemistry, catalysis, fuel, nuclear waste separation, electrochemistry, rocket propulsion, and pharmaceutical communities.⁵ A crucial property of ionic liquids is the possibility of *chemically tuning* their physical properties such as the melting point, density, radiation stability, and viscosity for the required application by synthesizing distinct anions, cations, and adding different functional groups.^{4,6}

The implementation of RTILs in rocket propulsion systems is a key area of intense research.⁷ Traditional rocket engines employ hydrazine (N₂H₄) and the dinitrogen tetroxide (N₂O₄) oxidizer as a hypergolic fuel—a propellant combination the components of which spontaneously ignite upon mutual contact.^{8,9} However, hydrazine has significant disadvantages including toxicity, high volatility, flammability, and a relatively low energy density of only 19 kJ cm⁻³ for combustion in oxygen.⁸ Consequently, hypergolic ionic liquids with a low vapor pressure, for example, 1-butyl-3-methylimidazolium dicyanamide ([BMIM][DCA]), which is pyrophoric with oxidizers like white-fuming nitric acid (HNO₃), have been synthesized to potentially replace hydrazine.^{7,10–12} These RTILs with potential energetic applications are known as energetic ionic liquids (EILs) and contain organic cations with a high nitrogen content such as imidazolium or triazolium to increase the energy density (Schemes 1 and 2);¹³ the incorporation of dicyanamide anions (Schemes 1 and 2) results in lower viscosities and hence reduced ignition times.^{7,14} Chambreau et al. combined aerosol generation with tunable vacuum ultraviolet (VUV) photoionization mass spectrometry to identify several products of the hypergolic reaction of [BMIM][DCA] with gaseous nitric acid (HNO₃) including carbon dioxide (CO₂), nitrous oxide (N₂O), and isocyanic acid (HNCO).¹⁵

The energy density of these EILs can be further enhanced by adding high energy-density solids. Boron represents an ideal additive,¹⁶ since it holds a higher energy density for combustion in oxygen (138 kJ cm⁻³) than alternative combustible metals such as aluminum (84 kJ cm⁻³) or magnesium (43 kJ cm⁻³) and traditional hydrocarbon fuels (35–40 kJ cm⁻³).¹⁷ However, a layer of boron oxide (B₂O₃) forms on the surface of boron when exposed to air, which inhibits ignition.^{18,19} This complication of utilizing boron as a high-energy additive is exacerbated by the high temperature of vaporization of boron at 4200 K, which results in chemical reactions occurring predominantly on the surface of a liquid. Consequently, the rate of combustion is severely limited by diffusion to and from the gas–liquid interface. Therefore, boron nanoparticles have been employed to increase the surface area-to-volume ratio and thereby reduce the limitation by diffusion; however, the mass fraction of the oxide layer increases as the diameter of the boron particles reduces. As a possible solution to the oxidation problem, Anderson et al. demonstrated that incorporating hydrogen-capped boron nanoparticles in air-stable ionic liquids such as [BMIM][DCA] and 1-methyl-4-amino-1,2,4-triazolium dicyanamide ([MAT]-

[DCA]) can prevent formation of oxide layers.^{20,21} Although stable in air, for application in hypergolic fuels, it is vital to understand the extent to which the passivation layer of these IL-capped boron nanoparticles can also resist oxidation by more reactive oxidizers such as dinitrogen tetroxide (N₂O₄) employed in bipropellants⁹ and nitrogen dioxide (NO₂).

Therefore, to significantly enhance the performance of hypergolic, EIL-based fuels, it is crucial to elucidate the underlying reaction mechanisms of EILs with the oxidizers. EILs composed of imidazolium or triazolium cations and dicyanamide anions (Schemes 1 and 2) are promising candidates for the next generation of hypergolic fuels.^{7,11,15,16} To this end, we previously explored spectroscopically the reaction between [MAT][DCA] (Schemes 1 and 2) and the oxidizer nitrogen dioxide (N₂O₄ ⇌ 2NO₂) and probed for one of the possible initial reaction intermediates, [O₂N–NCNCN]⁻.⁵ Here, we expand our studies on the oxidation and reactivity of levitated EIL droplets by comparing quantitatively the reactivity and rate constants of pure and boron-doped [BMIM][DCA] and [MAT][DCA] with nitrogen dioxide (NO₂). Both EILs contain the [DCA]⁻ anion, but the [BMIM]⁺ cation differs from the [MAT]⁺ cation by carrying a butyl chain (–C₄H₉) in place of the amino functional group (–NH₂) and having one nitrogen atom fewer in its imidazolium ring (Scheme 1). In addition to the rate constants, our spectroscopic investigations aim to identify the key initial intermediates and functional groups formed upon reaction of [BMIM][DCA] with nitrogen dioxide. Each system was explored with and without hydrogen-capped boron nanoparticles to investigate the possible (catalytic) oxidation processes of the boron and the effect on the reaction rate by the nanoparticles. These experiments were carried out for single, levitated droplets in an ultrasonic levitation device. Acoustic levitation of a single droplet of an EIL has several important advantages over traditional *bulk* experiments.^{22,23} Levitation avoids the complicating effects of a contacting surface, which permits the so-called container-less processing of a droplet. By enclosing the levitator within a pressure-compatible process chamber, a single droplet can be suspended in the reactive gas of interest at a well-defined temperature and pressure. Furthermore, for the present experimental layout with the droplet levitated in the center of the process chamber, complementary Raman (Ra), ultraviolet–visible (UV–Vis), and Fourier-transform infrared (FTIR) spectrometers can simultaneously probe for chemical modifications of the droplet in real time and *in situ*. The levitation device is thus ideally suited to study reactions between ionic liquids and oxidizers.

2. EXPERIMENTAL METHODS

The levitation experimental apparatus has been described in detail previously.^{22,23} The experiments exploit an acoustic levitator operated at a frequency of 58 kHz. Here, ultrasonic sound waves produced by a piezoelectric transducer placed at the bottom of the levitation device reflect from a concave-shaped plate to generate a standing wave.²² The sound waves exert acoustic radiation pressure on the droplet,²⁴ so that the droplet is levitated slightly below the pressure nodes of the standing wave. The levitator device is enclosed within a pressure-compatible process chamber, which enables levitation in an inert gas such as argon (Ar), or the introduction of highly reactive and toxic gases to study reactions between the gas and the levitated droplet. The present experiments were performed with either 98.7% argon (Ar) and 1.3% nitrogen dioxide

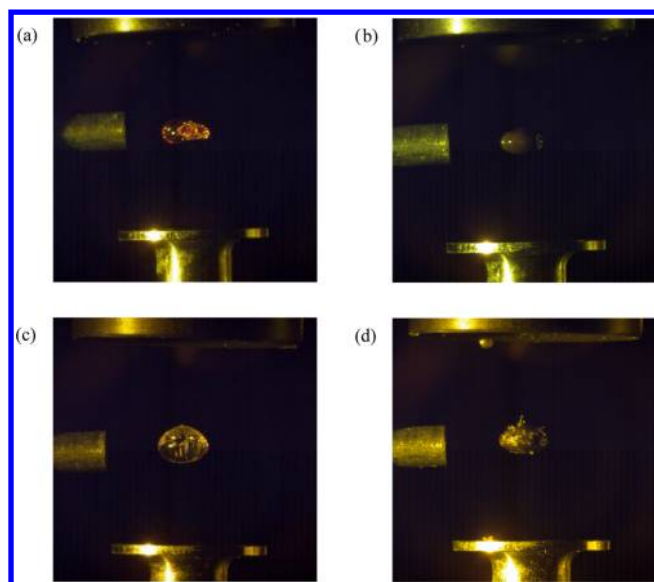


Figure 1. Photographs of droplets of (a) [BMIM][DCA], (b) boron-doped [BMIM][DCA], (c) [MAT][DCA], and (d) boron-doped [MAT][DCA] levitated in 1.3% nitrogen dioxide and 98.7% argon. Bubbles produced by the reaction between the ionic liquid and the oxidizer gas can be seen below the surfaces. The [MAT][DCA] droplet shown in (c) has enlarged significantly, and for the boron-containing [MAT][DCA] sample displayed in (d) crystal-like protrusions also appeared above the surface. The yellowish hue is caused by the nitrogen dioxide.

(NO₂) or 99.8% Ar and 0.2% NO₂. The temperature and total pressure of the gas in the chamber were 298 K and 880 Torr, respectively.

To levitate droplets with diameters of typically 2 mm, we incorporated a microliter droplet deposition system. A syringe is interfaced via a vacuum-compatible valve to a conflat flange on the outside port of an ultra-high vacuum chamber. The valve allows the main chamber to be evacuated and then filled with the required process gas before levitating a droplet. Inside the chamber, the valve is connected via chemically inert polyetheretherketone (PEEK) tubing to a microneedle which, in turn, is attached to the end of a wobble stick. The wobble stick is fixed to the side port located above the syringe and enables full translational motion of the needle and rotation about its central axis. The flexible tubing permits the needle to be moved to the center of the chamber to levitate the droplet and the deposition device to be withdrawn prior to the spectroscopic measurements.

The levitated droplet can be heated to the desired temperature by the output of a 40 W carbon dioxide laser emitting at 10.6 μm (Synrad Firestar v40). The output power of the laser can be adjusted between 1 and 40 W by varying the duty cycle of the discharge. A planar copper mirror and zinc selenide (ZnSe) window on the chamber transport the infrared beam to the levitated particle. The temperature of the levitated droplet is determined by a thermal imaging camera (FLIR A6703sc). The camera employs a cooled detector composed of 640 \times 512 pixels, which covers the spectral range from 3 to 5 μm . This system can determine temperatures between 253 and 1773 K with an accuracy of $\pm 2\%$ of the reading. When a 50 mm lens with a 12.7 mm extender ring is used, the effective pixel size produced on the droplet at the working distance of 220 mm is 56 μm . Consequently, there are 18 pixels across a 1

mm diameter droplet, which exceeds the 10-pixel minimum required for accuracy.

To characterize the chemical and physical changes of the levitated droplet, the chamber is interfaced to complementary, high-sensitivity Raman, FTIR, and UV–Vis spectroscopic probes. The Raman transitions are excited by the 532 nm line of a diode-pumped, Q-switched Nd:YAG laser.²⁵ The Raman-shifted photons, backscattered from the droplet, are focused by a lens into a HoloSpec $f/1.8$ holographic imaging spectrograph equipped with a CCD camera (Princeton Instruments PI-Max 2 ICCD). Two overlaid holographic transmission gratings simultaneously cover the spectral ranges from 170 to 2450 cm^{-1} and 2400 to 4400 cm^{-1} with a resolution of 9 cm^{-1} . The apparatus can also collect infrared spectra from 400 to 4000 cm^{-1} in the region of a levitated droplet *in situ* by employing a Thermo Scientific Nicolet 6700 FTIR spectrometer. To increase the detection efficiency, the infrared beam is focused by two stages of mirror optics to a diameter of 4 mm in the region of the droplet. The transmitted IR radiation subsequently enters an identical optical system in the reverse order, so that the original unfocused IR beam is recovered before entering the liquid-nitrogen cooled, MCT-B (mercury cadmium telluride, wide-band) IR detector. The infrared spectra of liquids can also be recorded by an attenuated total reflection (ATR) accessory located within the FTIR spectrometer. Finally, within a Hamamatsu L10290 UV–visible fiber light source, the outputs from a high-brightness deuterium lamp and tungsten-halogen lamp combine to produce radiation in the 200–1600 nm wavelength range. The output from the UV–Vis source is transmitted via a fiber-optic feedthrough on a conflat flange to a Y-type reflectance probe located inside of the process chamber. In the reflectance probe, seven 400 μm diameter illuminating fibers surround one 600 μm diameter read fiber. An optional half-ball lens can be attached to the end of the probe to focus the beam onto the droplet and, hence, significantly increase the detection efficiency. The probe end is attached to an xyz manipulator, so that the fiber optics can be positioned to maximize the count rate. The light backscattered by the droplet is collected by the read fiber, exits the chamber via a second connector on the same conflat fiber-optic feedthrough, and lastly enters a StellarNet SILVER-Nova UV–visible spectrometer. The spectrometer covers the 200–1100 nm spectral range and provides a resolution of 2 nm with the 50 μm entrance slit. The sensitivity of the spectrometer system versus wavelength was calibrated using a UV-enhanced aluminum mirror with an accurately known reflectance in the relevant spectral region (Thorlabs Inc., part number: PFSQ05-03-F01).

In our studies, the oxidation processes can occur over time scales as short as a few tens of milliseconds.¹⁶ To document such high-speed events, a Phantom Miro 3a10 camera is interfaced to the levitator. This camera can record up to 1850 frames per second at the maximum resolution of 1280 \times 1280 pixels and is capable of exposure times as short as 1 μs . To zoom-in on the small droplet and thereby study in detail the visual changes induced by the chemical reactions, a Navitar Zoom 6000 modular lens system is attached to the camera. The field of view (FOV) can be reduced from 28 mm \times 28 mm to 4.4 mm \times 4.4 mm at the camera–droplet distance of 220 mm. The lowest field of view corresponds to a full angle of only 1.1 $^\circ$ and consequently gives the required high-resolution images of the droplets. By calibrating the length scale using an

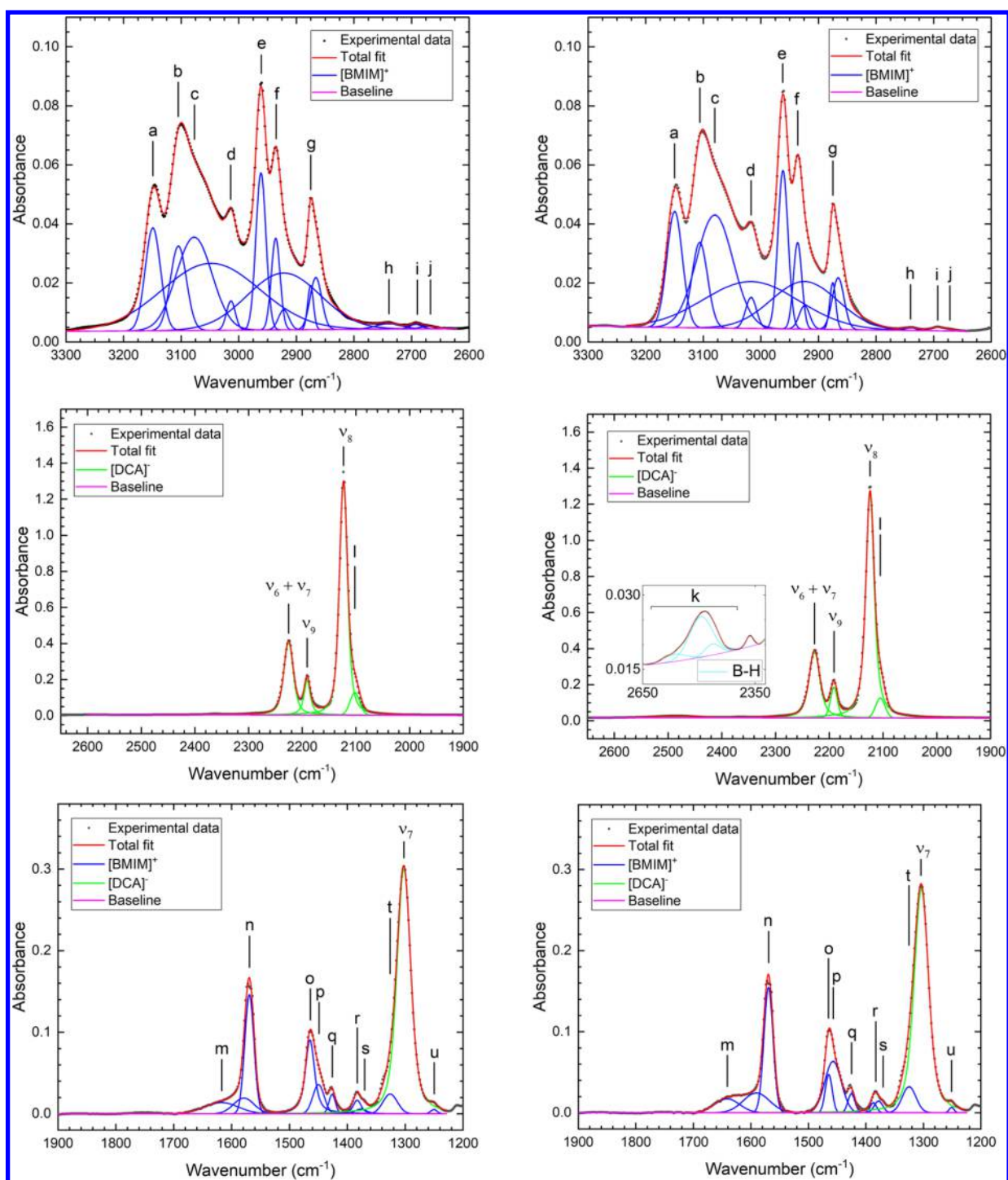


Figure 2. continued

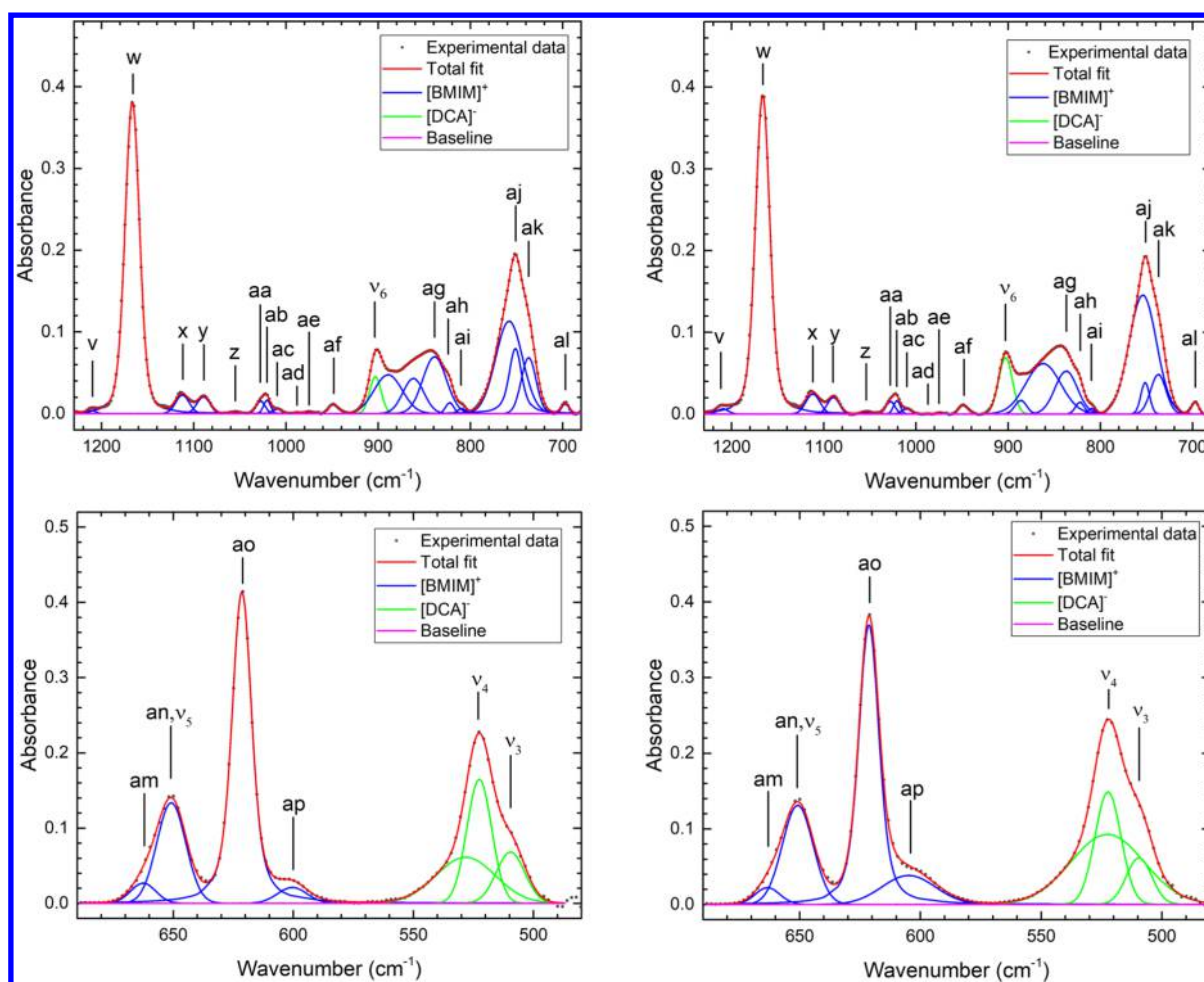


Figure 2. FTIR spectra and individual peak fits of [BMIM][DCA] (left column) and [BMIM][DCA] with hydrogen-capped boron nanoparticles (right column). The vibrational assignments for the [BMIM]⁺ and [DCA]⁻ peaks labeled a–ap and ν_3 – ν_6 , respectively, are given in Table 1. The background has been subtracted from the spectra to display the peaks with improved clarity.

object of known dimensions, the small FOV of the camera also enables the size of the droplet to be determined precisely.

[BMIM][DCA] was purchased from IoLiTec Inc. with a purity greater than 98%. The boron nanoparticles were produced by first high-energy ball-milling boron powder in a hydrogen atmosphere, resulting in hydrogen-terminated nanoparticles, and then capping with [BMIM][DCA] to generate air-stable, unoxidized particles.²⁶ The boron-doped [BMIM]-[DCA] studied in the present experiments was prepared by adding 5% by weight of the boron nanoparticles so produced to the pure ionic liquid. Photographs of droplets of [BMIM][DCA], boron-doped [BMIM][DCA], [MAT]-[DCA], and boron-doped [MAT][DCA] levitated in 1.3% NO₂ and 98.7% Ar are shown in Figure 1. Bubbles produced by the reaction between the ionic liquid and the oxidizer gas can be seen below the surfaces of the droplets.

3. RESULTS AND DISCUSSION

3.1. [BMIM][DCA]. **3.1.1. Infrared Spectroscopy.** To identify the newly formed peaks in the spectra following reaction with the oxidizer, it is first necessary to collect and interpret the spectra of the unreacted ionic liquids as references. The ATR-FTIR spectra of pure and boron-doped [BMIM][DCA] are shown in Figure 2. The curve fits to decompose the spectra into the component peaks are included

in Figure 2 with the resulting peak wavenumbers compiled in Table 1.^{27–30} In some regions of the spectra with many overlapping peaks, there is a significant degeneracy or nonuniqueness in the fitting procedure. Therefore, we only report the optimized peak wavenumbers for clearly defined peaks or prominent shoulders. Furthermore, the fitted peaks are observed superimposed on broad backgrounds produced by the operation of the ATR-FTIR spectrometer. The backgrounds were modeled by optimizing a polynomial of fifth to eighth order simultaneously with the parameters for the peaks.

To assign the vibrational modes to the peaks in the spectra, the fitted wavenumbers were compared with the measured and theoretical values for similar ionic liquids published in the literature.^{27–29} The vibrational modes for ionic liquids containing 1-alkyl-3-methylimidazolium cations have been extensively studied by means of quantum chemistry calculations. In this section, we use the common notation for 1-alkyl-3-methylimidazolium cations, [C_nC₁im]⁺, where the subscripts *n* and 1 denote the number of carbon atoms in the alkyl chains attached to the imidazolium ring (im). Berg applied MP2 calculations to determine the vibrational frequencies for the isolated [C₄C₁im]⁺ (or [BMIM]⁺) cation with the butyl chain in the anti-anti (AA) or gauche-anti (GA) conformations.³¹ Density functional theory (DFT) in combi-

Table 1. Wavenumbers and Vibrational Modes for the Observed Peaks in the FTIR Spectra of [BMIM][DCA] and [BMIM][DCA] with Hydrogen-Capped Boron Nanoparticles^a

peak label ^b	vibrational mode ^c	reference wavenumbers [measured ^m , theoretical ^t] (cm ⁻¹)	present measured wavenumbers [BMIM][DCA] (cm ⁻¹) ^d	present measured wavenumbers boron-doped [BMIM][DCA] (cm ⁻¹) ^d
a	$\nu(\text{C4-H}), \nu(\text{C5-H})$ out-of-phase	3163 ^m 3160–3163 ^t	3149	3150
	$\nu(\text{C4-H}), \nu(\text{C5-H})$ in-phase	3178–3183 ^t		
b		3123 ^m	3105	3106
	$\nu(\text{C2-H})$	3122–3152 ^t		
c	no assignment ²⁷	3105 ^m	3078 ± 6	3080 ± 5
d			3015	3017
	$\nu_{\text{as}}[\text{CH}_3(\text{Me})]$	3004–3030 ^t		
e		2966 ^m	2963	2962
	$\nu_{\text{as}}(\text{CH}_2)$	2957–2983 ^t		
f		2942 ^m	2936 ± 3	2936 ± 2
	$\nu_{\text{as}}(\text{CH}_2)$	2934–2943 ^t		
g		2878 ^m	2875	2875
	$\nu_{\text{s}}[\text{CH}_3(\text{Bu})]$	2869–2886 ^t		
h	combination band, e.g., ($\nu_6 + \nu_7$) + ν_4 or n + w		2740	2740
i	combination band, e.g., $\nu_3 + \nu_9$		2690	2693
j	combination band, e.g., $\nu_4 + \nu_8$		2667	2672
k	B–H	2480–2565 ³⁰		≈2400–2640
$\nu_6 + \nu_7$	Fermi enhanced $\nu_{\text{s}}(\text{N–C})$ + $\nu_{\text{as}}(\text{N–C})$ combination band	2228 ²⁹	2225	2228
ν_9	$\nu_{\text{s}}(\text{C}\equiv\text{N})$ (A ₁)	2192 ²⁸	2191	2191
ν_8	$\nu_{\text{as}}(\text{C}\equiv\text{N})$ (B ₂)	2133 ²⁸	2123	2124
l	$\nu(\text{C–N})$	2102 ²⁹	2102	2105 ± 2
m	no assignment ²⁷		1617	1641 ± 6
n		1568 ^m	1569	1569
	$\nu_{\text{as}}(\text{N1C2N3}), r(\text{C2–H})$	1563–1575 ^t		
		1575 ^m		
	$\nu(\text{C=C})$	1581–1584 ^t		
o		1467 ^m	1465	1465
	$\delta_{\text{s}}(\text{CH}_3)$	1470–1474 ^t		
p		1454 ^m , 1459 ^m	1450	1457
	$\delta_{\text{s}}(\text{CH}_2)$	1446–1454 ^t		
	$\delta_{\text{as}}[\text{CH}_2(\text{Me})]$	1450–1457 ^t		
	$\delta_{\text{s}}(\text{CH}_2)$	1455–1458 ^t		
q		1431 ^m	1426	1425
	$\delta_{\text{s}}[\text{CH}_3(\text{Me})]$	1430–1432 ^t		
r		1387 ^m	1383	1383
	w(CH ₂)	1383–1395 ^t		
s		1373 ^m	1370	1370
	$\nu(\text{C2N1C5}), w(\text{CH}_2)$	1369–1387 ^t		
t		1339 ^m	1326	1325 ± 7
	breathing, $\nu(\text{N–Bu}), \nu(\text{N–Me})$	1330–1359 ^t		
ν_7	$\nu_{\text{as}}(\text{N–C})$ (B ₂)	1309 ²⁸	1302	1304
u		1253 ^m	1250	1251
	t(CH ₂), r(C2–H)	1255–1260 ^t		
v		1213 ^m	1210 ± 3	1210 ± 2
	t(CH ₂)	1214–1222 ^t		
w		1172 ^m	1167	1166
	$\nu(\text{N–Bu}), \nu(\text{N–Me}), r(\text{C–H})$	1153–1165 ^t		
x		1116 ^m	1112	1112
	r(CH ₃), r[CH ₃ (Bu)]	1103–1116 ^t		
y		1093 ^m	1090	1090
		(Raman)		
	r(CH)	1090–1091 ^t		
	r(CH ₃), r[CH ₃ (Bu)]	1106–1193 ^t		
z			1055	1054
	$\nu(\text{C–C}), r(\text{C–H})$	1051–1071 ^t		
	$\nu(\text{C–C})$	1066 ^t		

Table 1. continued

peak label ^b	vibrational mode ^c	reference wavenumbers [measured ^m , theoretical ^t] (cm ⁻¹)	present measured wavenumbers [BMIM][DCA] (cm ⁻¹) ^d	present measured wavenumbers boron-doped [BMIM][DCA] (cm ⁻¹) ^d
aa	$\nu(\text{C—C})$	1037 ^m 1039–1046 ^t	1028	1028
ab	δ ring	1022–1036 ^t	1021	1021
ac	breathing, $\nu(\text{N—Bu})$, $\nu(\text{N—Me})$	1015–1020 ^t	1010	1010
ad	$\gamma(\text{C—H})$	992 ^m 982–983 ^t	988	987
ae	$\nu_{\text{as}}(\text{C—C})$	975 ^m 954–976 ^t	975	975
af	$r[\text{CH}_3(\text{Bu})]$, $r(\text{CH}_2)$	948 ^m 945, 973 ^t	948	948
ν_6	$\nu_s(\text{N—C}) (A_1)$	904 ²⁸	903	903
ag	$\gamma(\text{C4—H})$, $\gamma(\text{C5—H})$	849 ^m 813–815 ^t	839 ± 9	837 ± 2
ah	$\nu_s(\text{C—C—C})$	835 ^m 805, 807 ^t	823	822
ai	$\nu_s(\text{C—C—C})$	808 ^m 785–796 ^t	810 ± 3	810
aj	$r(\text{CH}_2)$	755 ^m 741–760 ^t	751	751
ak	$r(\text{CH}_2)$	737 ^m 731 ^t	737	737
al	$\nu(\text{N—Me})$, $\nu(\text{N—Bu})$	697 ^m 686–692 ^t	697	697.3
am	$\nu(\text{N—Me})$, $\nu(\text{N—Bu})$	660 ^m 672 ^t	663 ± 4	663 ± 2
an	$\gamma(\text{N—Me})$, $\gamma(\text{N—Bu})$	651 ^m 656–662 ^t	651	651
ν_5	$\delta(\text{CNC}) (A_1)$	666 ²⁸		
ao	$\gamma(\text{N—Bu})$, ring-puckering	623 ^m 625–634 ^t	621	
ap	$\delta(\text{N1—C2—N3})$	600 ^m 582–595 ^t	600	605
ν_4	$\gamma_s(\text{N—C}\equiv\text{N}) (A_2)$	524 ²⁸	523	522
ν_3	$\gamma_{\text{as}}(\text{N—C}\equiv\text{N}) (B_1)$	508 ²⁸	510	509

^aThe assignments were performed for the [BMIM]⁺ cation using the theoretical calculations^t and measurements^m of ref 27, for the [DCA]⁻ anion by comparison with the measured values of ref 28 and ref 29, and ref 30 for the B–H modes. ^bThe letters a–ap correspond to the [BMIM]⁺ peak labels in Figure 2 and ν_3 – ν_9 are the vibrational mode numbers of the [DCA]⁻ anion. ^cKey: ν , stretch; δ , bend; w, wagging; t, twisting; r, rocking; γ , out-of-plane; s, symmetrical; as, antisymmetrical. ^dThe quoted errors combine the uncertainties from determining the peak wavenumbers in the fitting procedure and calibrating the wavenumber scale. The uncertainties are equal to, or less than, 1 cm⁻¹ unless stated otherwise.

nation with a 6-31+G(d,p) basis set and a B3LYP functional was employed by Talaty et al.³² to calculate the vibrational frequencies for the [C_nC₁im][PF₆] ionic pair, and by Heimer et al.³³ and Katsyuba et al.²⁷ for [C_nC₁im][BF₄], where $n = 2, 3$, or 4. Holomb et al.³⁴ used similar ab initio calculations and Raman spectroscopy measurements to study [C₄C₁im][BF₄] and thereby identified the four conformers GG, AG, AA, and GA in the room-temperature ionic liquid. However, to our knowledge, a corresponding detailed experimental or theoretical study has not been performed for the [C₄C₁im]⁺ and [DCA]⁻ ionic pair ([BMIM][DCA]). After accounting for small shifts in the peak positions produced by having a [DCA]⁻ anion in place of a [BF₄]⁻ anion, we found our [BMIM]⁺ wavenumbers corresponded with sufficient accuracy to the values for [BMIM]⁺ in [BMIM][BF₄] as measured and calculated by Katsyuba et al.²⁷ to permit assignments in most regions of the spectra. In Table 1, the present [BMIM]⁺ peaks are therefore assigned in accordance with ref 27. The

vibrational mode numbers ν_1 – ν_{75} are unavailable in ref 27, and therefore the peaks and corresponding vibrational modes of the [BMIM]⁺ cation are labeled by the letters a–ap in Table 1 and Figure 2. The range of theoretical wavenumbers for each vibrational assignment in Table 1 is a consequence of the six different conformations of the butyl chain accounted for in the calculations. The vibrational modes ν_3 – ν_9 for the [DCA]⁻ peaks were assigned by comparison with the observed infrared and Raman spectra of [C₂C₁im]⁺[DCA]⁻.^{28,29}

The different types of vibrational modes of the [BMIM]⁺ cation generally occur in multiple spectral regions. In the high-wavenumber range, the bands from 2800 to 3030 cm⁻¹ are attributed to the C–H stretching modes of the methyl and butyl groups attached to the imidazolium ring. From 3030 to 3200 cm⁻¹, the C–H stretching modes are associated with the imidazolium ring, for example, the peaks at 3105 and 3150 cm⁻¹ are produced by the C(2)–H and C(4),(5)–H stretching modes, respectively. In the 600–1600 cm⁻¹ region,

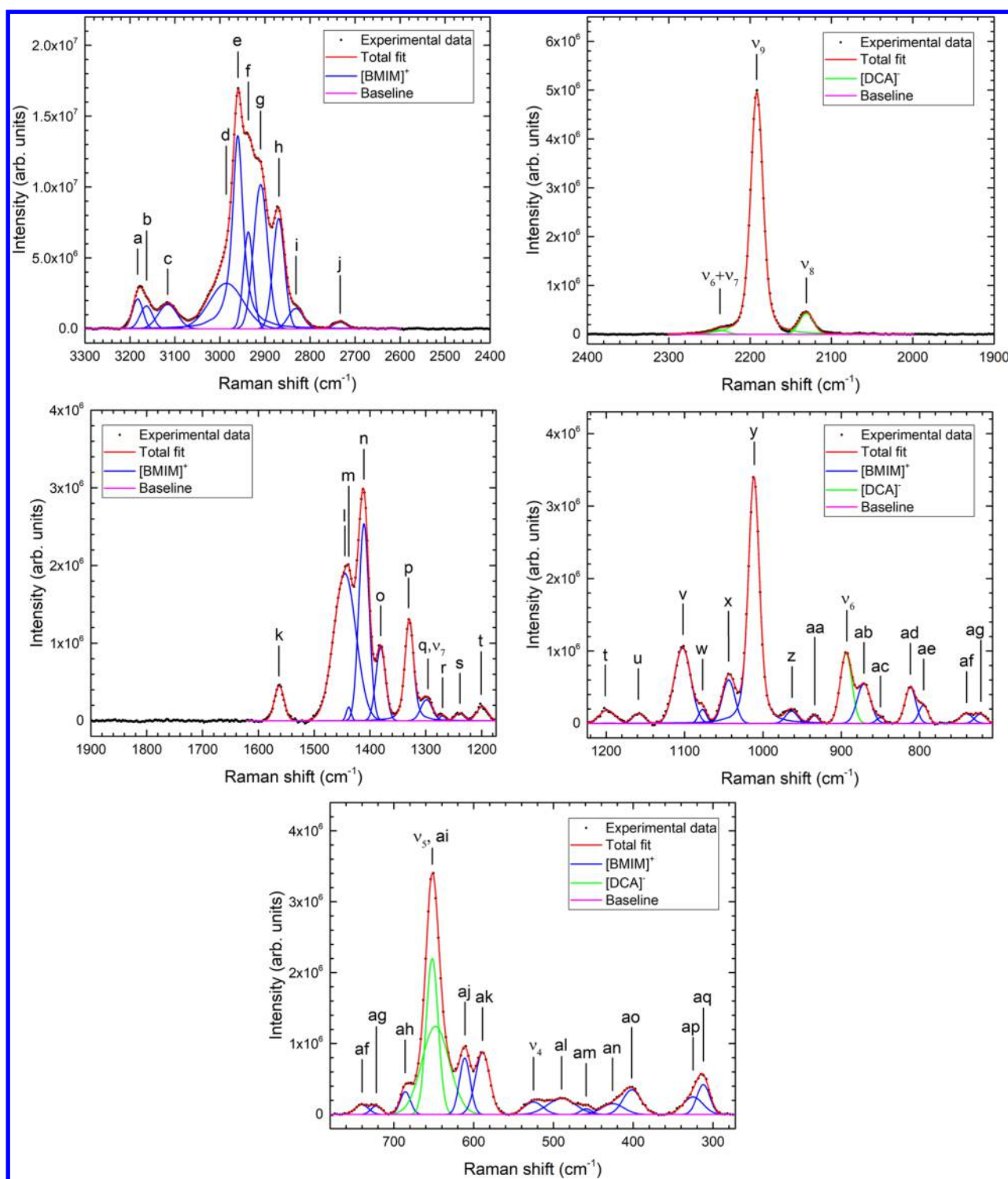


Figure 3. Raman spectra and individual peak fits of a [BMIM][DCA] droplet levitated in argon. The vibrational assignments for the [BMIM]⁺ and [DCA]⁻ peaks labeled a–aq and ν_4 – ν_9 , respectively, are given in Table 2. The background has been subtracted from the spectra to display the peaks with improved clarity.

vibrations of the imidazolium ring produce multiple overlapping peaks, for instance, those at 1010, 1325, 1370, and 1568 cm^{-1} are associated with the ac, t, s, and n ring modes, respectively (Table 1). In the lower-wavenumber range from 600 to 800 cm^{-1} , in addition to the ring vibrations, the methyl and butyl groups contribute significantly to the spectrum. Regarding the [DCA]⁻ anion, the peaks at 2126, 2197, and 2237 cm^{-1} are intense spectral features, which are assigned to

the asymmetric stretching mode $\nu_{\text{as}}(\text{C}\equiv\text{N})$, symmetric stretching mode $\nu_{\text{s}}(\text{C}\equiv\text{N})$, and the $\nu_{\text{s}}(\text{C}-\text{N}) + \nu_{\text{as}}(\text{C}-\text{N})$ combination band, respectively.^{28,29} The [DCA]⁻ anion also produces the relatively small peak at 903 cm^{-1} due to the ν_5 mode, and a broader structure between 500 and 550 cm^{-1} arising from the merged ν_3 and ν_4 peaks. The weak absorption at 2490 cm^{-1} is unique to the boron-doped sample and is assigned to the $\nu(\text{B}-\text{H})$ stretching mode.³⁰

Table 2. Wavenumbers and Vibrational Modes for the Observed Peaks in the Raman Spectrum of [BMIM][DCA]^a

peak label	vibrational mode ^b	reference wavenumbers [measured ^m , theoretical ^l] (cm ⁻¹)	present measured wavenumbers [BMIM][DCA] (cm ⁻¹) ^c
a	$\nu(\text{C4—H,C5—H})$ in-phase	3173 ^m 3178–3183 ^t	3183 ± 1
b	$\nu(\text{C4—H,C5—H})$ out-of-phase	3157 ^m 3160–3163 ^t	3163 ± 4
c	$\nu(\text{C2—H})$	3127 ^m 3122–3152 ^t	3116 ± 1
d	$\nu_{\text{as}}[\text{CH}_3(\text{Me})]$	3001 ^m 2982–3020 ^t	2986 ± 7
e	$\nu_{\text{as}}(\text{CH}_2)$	2969 ^m 2957–2983 ^t	2960 ± 1
f	$\nu_{\text{as}}(\text{CH}_2)$	2942 ^m 2934–2943 ^t	2937 ± 2
g	$\nu_{\text{s}}[\text{CH}_3(\text{Me})]$ $\nu_{\text{s}}[\text{CH}_3(\text{Me})]$ $\nu_{\text{as}}(\text{CH}_3), \nu_{\text{as}}(\text{CH}_2)$	2917 ^m 2902–2910 ^t 2904–2918 ^t 2912–2936 ^t	2910 ± 1
h	$\nu_{\text{s}}(\text{CH}_2)$ $\nu_{\text{s}}[\text{CH}_3(\text{Bu})]$	2877 ^m 2857–2874 ^t 2869–2886 ^t	2869 ± 1
i	$\nu_{\text{s}}(\text{CH}_2)$	2840 ^m 2840–2850 ^t	2832 ± 2
j	combination band, e.g., n + p		2733 ± 1
$\nu_6 + \nu_7$	Fermi enhanced $\nu_{\text{s}}(\text{N—C}) + \nu_{\text{as}}(\text{N—C})$ combination band	2228 ²⁹	2237 ± 2
ν_9	$\nu_{\text{s}}(\text{C}\equiv\text{N})$ (A ₁)	2192 ²⁸	2192 ± 1
ν_8	$\nu_{\text{as}}(\text{C}\equiv\text{N})$ (B ₂)	2133 ²⁸	2131 ± 1
k	$\nu_{\text{as}}(\text{N1C2N3}), r(\text{C2—H})$	1568 ^m 1563–1575 ^t	1563 ± 1
l	$\delta_{\text{s}}(\text{CH}_2)$ $\delta_{\text{as}}[\text{CH}_2(\text{Me})]$ $\delta_{\text{s}}(\text{CH}_2)$	1448 ^m 1446–1454 ^t 1450–1457 ^t 1455–1458 ^t	1445 ± 1
m	$\delta_{\text{s}}(\text{CH}_2)$	1439–1447 ^t	1438 ± 1
n	$\delta_{\text{s}}[\text{CH}_3(\text{Bu})]$ $\nu_{\text{ring}}, \delta(\text{CH}_2)$	1421 ^m 1397–1407 ^t 1417–1421 ^t	1411 ± 1
o	$\nu_{\text{as}}(\text{C2N1C5}), w(\text{CH}_2)$ $w(\text{CH}_2)$	1391 ^m 1369–1387 ^t 1383–1395 ^t	1381 ± 1
p	breathing, $\nu(\text{N—Bu}), \nu(\text{N—Me})$	1342 ^m 1330–1359 ^t	1329 ± 1
q	$t(\text{CH}_2)$	1303 ^m 1293–1312 ^t 1311 ^m	1299 ± 1
ν_7	$\nu_{\text{as}}(\text{N—C})$ (B ₂)	1315–1328 ^t 1309 ²⁸	
r	$r(\text{C—H}), t(\text{CH}_2)$ $r(\text{C—H}), t(\text{CH}_2)$	1286 ^m 1270–1273 ^t 1279–1287 ^t	1270 ± 2
s	$t(\text{CH}_2), r(\text{C2—H})$	1254 ^m 1255–1260 ^t	1239 ± 2
t	$r(\text{C2—H}), t(\text{CH}_2)$ $t(\text{CH}_2)$	1212 ^m 1199 ^t 1214–1222 ^t	1201 ± 1
u	$\nu(\text{N—Bu}), \nu(\text{N—Me}), r(\text{C—H})$	1173 ^m 1153–1165 ^t	1159 ± 2
v	$r(\text{CH}_3), r[\text{CH}_3(\text{Bu})]$ $r(\text{CH}_3), r[\text{CH}_3(\text{Bu})]$	1117 ^m 1093–1106 ^t 1103–1116 ^t	1102 ± 1
w		1093 ^m	1077 ± 1

Table 2. continued

peak label	vibrational mode ^b	reference wavenumbers [measured ^m , theoretical ^t] (cm ⁻¹)	present measured wavenumbers [BMIM][DCA] (cm ⁻¹) ^c
x	$\nu(\text{C—C})$	1069–1089 ^t	1044 ± 1
	$\nu(\text{C—C})$	1057 ^m	
y	$\nu(\text{C—C})$	1039–1046 ^t	1011 ± 1
	breathing, $\nu(\text{N—Bu})$, $\nu(\text{N—Me})$	1024 ^m	
z	$\nu(\text{C—C})$	1015–1020 ^t	963 ± 1
	$\nu_{\text{as}}(\text{C—C})$	976 ^m	
aa	$\gamma(\text{C2—H})$	954–976 ^t	934 ± 1
	$\gamma(\text{C2—H})$	951 ^m	
ν_6	$r[\text{CH}_3(\text{Bu})]$, $r(\text{CH}_2)$	926–929 ^t	894 ± 1
	$\nu_s(\text{N—C})$ (A ₁)	930–946 ^t	
ab	$\nu_s(\text{N—C})$ (A ₁)	945–973 ^t	871 ± 1
	$\nu(\text{C—C})$	904 ²⁸	
ac	$\nu(\text{C—C})$	884 ^m	850 ± 1
	$\nu(\text{C—C})$	870–878 ^t	
ad	no assignment ²⁷	874–894 ^t	812 ± 1
	$\nu_s(\text{C—C—C})$	825 ^m	
ae	$\gamma(\text{C4—H})$, $\gamma(\text{C5—H})$	805–807 ^t	795 ± 1
	$\nu_s(\text{C—C—C})$	813–815 ^t	
af	$r(\text{CH}_2)$	810 ^m	740 ± 2
	$\nu_s(\text{C—C—C})$	785–796 ^t	
ag	$r(\text{CH}_2)$	741–760 ^t	722 ± 2
	$\nu(\text{N—Me})$, $\nu(\text{N—Bu})$	734 ^m	
ah	$\gamma(\text{C4—H})$, $\gamma(\text{C5—H})$	724 ^t	686 ± 1
	$r(\text{CH}_2)$	722–724 ^t	
ai	$\nu(\text{N—Me})$, $\nu(\text{N—Bu})$	731 ^t	652 ± 1
	$\gamma(\text{N—Me})$, $\gamma(\text{N—Bu})$	699 ^m	
aj	$\delta(\text{CNC})$ (A ₁)	686–692 ^t	611 ± 1
	$\gamma(\text{N—Bu})$, ring puckering	651 ^m	
ak	$\delta(\text{N1—C2—N3})$	656–662 ^t	589 ± 1
	$\gamma_s(\text{N—C}\equiv\text{N})$ (A ₂)	666 ²⁸	
al	$\delta(\text{N—C—C})$, $\delta(\text{C—C—C})$	624 ^m	490 ± 2
	$\delta(\text{N—C—C})$, $\delta(\text{C—C—C})$	625–634 ^t	
am	$\delta(\text{N—C—C})$, $\delta(\text{C—C—C})$	601 ^m	459 ± 2
	$\delta(\text{N—C—C})$, $\delta(\text{C—C—C})$	582–594 ^t	
an	$r(\text{N—Bu})$, $r(\text{N—Me})$, $\delta(\text{N—C—C})$, $\delta(\text{C—C—C})$	524 ²⁸	426 ± 9
	$r(\text{N—Bu})$, $r(\text{N—Me})$	501 ^m	
ao	$r(\text{N—Bu})$, $r(\text{N—Me})$, $\delta(\text{C—C—C})$	481–499 ^t	403 ± 3
	$r(\text{N—Bu})$, $r(\text{N—Me})$	473 ^m	
ap	$\delta(\text{C—C—C})$	465–476 ^t	325 ± 13
	$\delta(\text{N—Me})$, $\delta(\text{N—Bu})$	435 ^m	
aq	$\delta(\text{C—C—C})$	442 ^t	312 ± 1
	$\delta(\text{C—C—C})$	415 ^m	

^aThe assignments were performed for the [BMIM]⁺ cation using the theoretical calculations^t and measurements^m of ref 27, and for the [DCA]⁻ anion by comparison with measured values of ref 28 and ref 29. The letters a–aq correspond to the [BMIM]⁺ peak labels in Figure 3 and ν_4 – ν_9 are the vibrational mode numbers of the [DCA]⁻ anion. ^bKey: ν , stretch; δ , bend; w, wagging; t, twisting; r, rocking; γ , out-of-plane; s, symmetrical; as, antisymmetrical. ^cThe quoted errors combine the uncertainties from determining the peak wavenumbers in the fitting procedure and calibrating the wavenumber scale.

3.1.2. Raman Spectroscopy. The Raman spectra of a [BMIM][DCA] droplet levitated in argon are shown in Figure 3. The fits to the spectra are included in Figure 3 and the

optimized peak wavenumbers are compiled in Table 2.^{27–29} The excitation of the sample by the 532 nm laser beam causes fluorescence. The resulting broad backgrounds were modeled

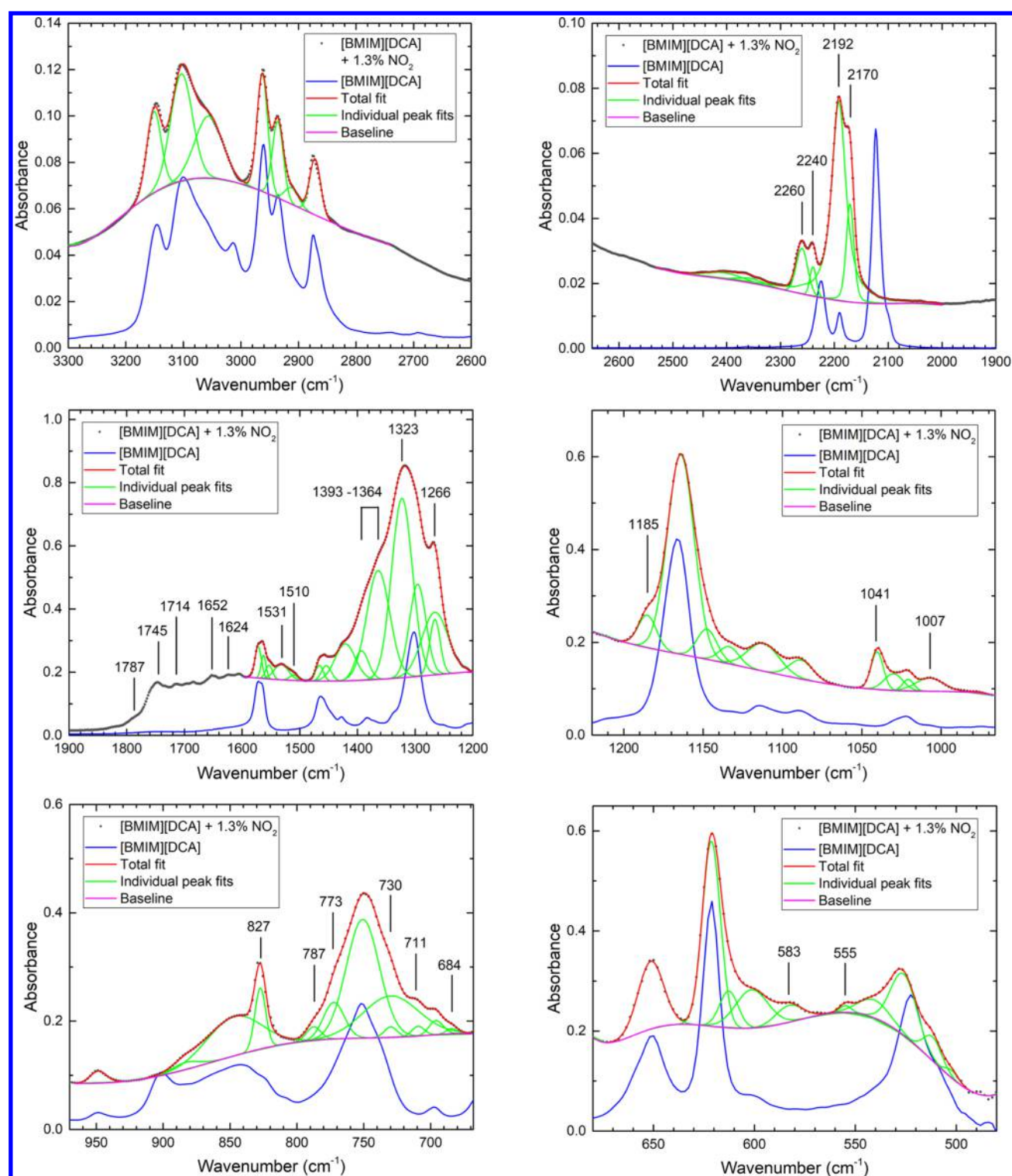


Figure 4. FTIR spectra and individual peak fits of [BMIM][DCA] after oxidation. The spectra of [BMIM][DCA] before the reaction are presented for comparison purposes (blue lines). The wavenumbers of the newly formed peaks are identified by the vertical lines, and the vibrational assignments are given in Table 3. The unreacted spectrum in the 2650–1900 cm^{-1} region has been scaled by the factor of 0.05.

by optimizing a polynomial simultaneously with the peak functions. The vibrational modes are assigned in Table 2 for the [BMIM]⁺ cation by comparison with ref 27 and for the [DCA]⁻ anion using the measurements of refs 28 and 29. The interpretation of the unreacted [BMIM][DCA] Raman spectrum will be used in section 3.2.2 when identifying the newly formed bands following reaction with nitrogen dioxide.

Owing to the different selection rules for infrared and Raman spectroscopy,³⁵ the relative amplitudes of the 75 fundamental modes of [BMIM][DCA] often differ significantly in their respective spectra (cf. Figures 2 and 3). For the [DCA]⁻ anion, the ν_3 , ν_4 , ν_7 , ν_8 , and $(\nu_6 + \nu_7)$ peaks are much smaller in the Raman than the infrared spectrum; whereas the ν_5 and ν_9 peaks are more prominent in the Raman spectrum than the

Table 3. Possible Assignments of Vibrational Modes for the New Peaks in the FTIR Spectra of a Pure or Boron-Doped [BMIM][DCA] Droplet Levitated in 1.3% NO₂ and 98.7% Ar^a

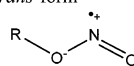
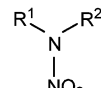
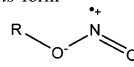
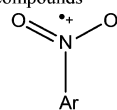
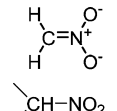
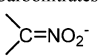
Measured wavenumber [BMIM][DCA] (cm ⁻¹)	Measured wavenumber boron-doped [BMIM][DCA] (cm ⁻¹)	Functional group or molecule	Region (cm ⁻¹)	Vibrational modes	Ref.
1787 ± 2	1788 ± 2	N ₂ O ₄	1791	a _g + b _{1g} , v ₄ + v ₅	36
1757 ± 8	1756 ± 8	N ₂ O ₄	1758	b _{2u} , v ₉	36
1745 ± 2	1743 ± 2			Two merged peaks	
1714 ± 2	1716 ± 2	N ₂ O ₄	1712	b _{1g} , v ₅	36
1652 ± 2	1649 ± 2	Organic nitrites, <i>trans</i> -form 	1680-1650 vs	N=O str. primary ~ 1675cm ⁻¹ , secondary ~ 1665cm ⁻¹ , tertiary ~ 1625cm ⁻¹ .	30
1624	1622	Nitroamines 	1630-1530 s	sym. NO ₂ str.	30
1624	1622	Organic nitrites, <i>cis</i> -form 	1625-1610 vs	N=O str. secondary ~ 1615 cm ⁻¹ , tertiary ~ 1610 cm ⁻¹ .	30
1532, 1510 ± 2	1622	Aromatic nitro-compounds 	1580-1485 s	asym. NO ₂ str.	30
1532, 1510 ± 2	1515	Nitroamines	1630-1530 s	asym. NO ₂ str.	30
1393 ± 2 - 1364 ± 7	1386 ± 3 - 1363 ± 3	Saturated primary and secondary aliphatic nitro-compounds 	1385-1360 vs	sym. NO ₂ str. (CH ₂ def. vib. also occurs in this region) Treat two peaks at ≈ 1390 cm ⁻¹ and ≈ 1360 cm ⁻¹ as a range.	30
1393 ± 2 - 1364 ± 7	1386 ± 3 - 1363 ± 3	Aromatic nitro-compounds	1370 - 1315 s	sym. NO ₂ str. For <i>o</i> - or <i>p</i> - strong electron donors from 1375-1285 cm ⁻¹ .	30
1323 ± 2	1317 ± 2	Aromatic nitro-compounds	1370 - 1315 s	sym. NO ₂ str. For <i>o</i> - or <i>p</i> - strong electron donors from 1375-1285 cm ⁻¹ .	30
1323 ± 2	1317 ± 2	Nitroamines	1315 - 1260 s	sym. NO ₂ str.	30
1266	1267	Carbonitrates 	1315 - 1205 s	asym. NO ₂ str.	30
1266	1267	Nitroamines	1315-1260 s	sym. NO ₂ str.	30
1185	1185	Pyridine N-oxides 	1190 - 1150 m-s		30
1041	1040	Aromatic nitro-compounds	1180 - 865 m	CN str.	30
1041	1040	Carbonitrates	1175 - 1040 s	sym. NO ₂ str.	30
1007	1008	Aromatic nitro-compounds	1180 - 865 m	CN str.	30
1007	1008	Nitroamines	1030 - 980 m	N-N str.	30
827	827	Organic nitrites, <i>cis</i> -form	850 - 810 s	N-O str.	30
790 ± 10	786 ± 2	Aromatic nitro compounds	790 - 690 s	Not always present	30
790 ± 10	786 ± 2	Organic nitrites, <i>trans</i> -form	815 - 750 vs	N-O str.	30

Table 3. continued

Measured wavenumber [BMIM][DCA] (cm ⁻¹)	Measured wavenumber boron-doped [BMIM][DCA] (cm ⁻¹)	Functional group or molecule	Region (cm ⁻¹)	Vibrational modes	Ref.
773	772	Nitroamines	775 - 755 w-m	NO ₂ def. vib.	30
773	772	Nitrites, <i>trans</i> -form	815 - 750 vs	N-O str.	30
740 ± 10	730 ± 10	Nitroamines	730-590 w-m	NO ₂ wagging vib.	30
740 ± 10	730 ± 10	Carbonitrates	735 - 700 m-s	NO ₂ def. vib.	30
680 ± 10	680 ± 10	Nitroamines	730 - 590 w-m	NO ₂ wagging vib.	30
680 ± 10	680 ± 10	Nitrites, <i>cis</i> -form	690 - 615 s	O-N=O def. vib.	30
583 ± 4	580 ± 20	Aromatic nitro compounds	590 - 500 v	In-plane bending vib. of -NO ₂ group	30
583 ± 4	580 ± 20	Nitroamines	620-560 w	NO ₂ rocking vib.	30
583 ± 4	580 ± 20	Nitrites, <i>trans</i> -form	625 - 565 s	O-N=O def. vib.	30
555	554	Saturated primary and secondary aliphatic nitro compounds.	560-470 m-s	NO ₂ rocking vib.	30

^aThe measured wavenumbers are from the present experiments, whereas the functional groups, regions of maximum absorption, IR intensities, and vibrational modes are from ref 30. Key: vs = very strong, s = strong, m = medium, w = weak, p = polarized. The quoted errors combine the uncertainties from determining the peak wavenumbers in the fitting procedure and calibrating the wavenumber scale. The uncertainties are equal to, or less than, 1 cm⁻¹ unless stated otherwise.

infrared spectrum; and for the ν_6 mode the peaks are of comparable amplitudes in both spectra. The vibrational modes of the imidazolium ring are generally enhanced in the Raman spectra, for example, the breathing $+\nu(\text{N}-\text{Bu}) + \nu(\text{N}-\text{Me})$, breathing $+\nu(\text{N}-\text{Bu}) + \nu(\text{N}-\text{Me})$, and $\delta_s[\text{CH}_3(\text{Bu})] + \nu_{\text{ring}} + \delta(\text{CH}_2)$ vibrational modes of the imidazolium ring at 1011, 1329, and 1411 cm⁻¹, respectively (Table 2). In the alkyl group C–H stretching region between 2800 and 3030 cm⁻¹, except for the one additional Raman peak labeled g at 2910 cm⁻¹, the infrared and Raman spectra are very similar. In contrast, in the ring C–H stretching region from 3030 to 3200 cm⁻¹, the broad structure in the FTIR spectrum formed by the overlap of peaks a to d is significantly enhanced compared to the corresponding structure in the Raman spectrum. Finally, we note that the peaks at 621, 751, and 1166 cm⁻¹ produced by the $\gamma(\text{N}-\text{Bu})$, $r(\text{CH}_2)$, and $\nu(\text{N}-\text{Bu}) + \nu(\text{N}-\text{Me}) + r(\text{C}-\text{H})$ modes, respectively, show higher intensities in the FTIR spectra, whereas the peak at around 1102 cm⁻¹ corresponding to the $r(\text{CH}_3) + r(\text{CH}_3(\text{Bu}))$ mode is significantly larger in the Raman spectrum.

3.2. [BMIM][DCA] Oxidation. **3.2.1. Infrared Spectroscopy.** We next discuss the oxidation of [BMIM][DCA] by nitrogen dioxide. After levitating the droplet in 1.3% NO₂ and 98.7% Ar, the reaction products were transferred to the ATR-FTIR spectrometer. The resulting FTIR spectra are shown in Figure 4 together with the individual peak fits and the spectrum of unreacted [BMIM][DCA] (blue line) for comparison. The reaction between the [BMIM][DCA] and nitrogen dioxide produced numerous new peaks in the spectrum at the wavenumbers listed in Table 3.^{30,36} The newly formed peaks were identified by comparing the spectra and individual peak fits before and after reaction of [BMIM][DCA] with the oxidizer (Figure 4). For complex organic molecules such as the oxidized ILs, infrared spectroscopy rarely enables identification of the individual, oxidized

molecules. However, infrared spectroscopy is a powerful tool to identify the *functional groups* emerging in the oxidation process. The simplest mechanism to form the new structure would involve the nitrogen or oxygen atom of the nitrogen dioxide reactant bonding to a carbon or nitrogen atom of [BMIM][DCA]. In Table 3, we therefore list functional groups of organic nitro-compounds with ranges of absorption that include the measured wavenumbers of the new peaks.³⁰ These assignments reveal that a surprisingly narrow range of organic nitro-compounds can account for the new structure including organic nitrites (RONO), nitroamines (RR'NNO₂), aromatic nitro-compounds (ArNO₂), and carbonitrates (RR'C=NO₂⁻). The most intense absorption at 1323 cm⁻¹ can be accounted for by the symmetric NO₂ stretch of the nitroamines or aromatic nitro-compounds. The corresponding ATR-FTIR spectrum and individual peak fits for an oxidized [BMIM][DCA] droplet doped with hydrogen-capped boron nanoparticles are shown in Figure 5. The oxidizer gas has produced essentially the same new structures as for the pure [BMIM][DCA] sample, and therefore the appearance of the new peaks can be attributed to nitrogen dioxide bonding to the ions of [BMIM][DCA] to form nitro-compounds instead of an initial reaction of nitrogen dioxide with the boron-based nanoparticles. The measured peak wavenumbers and vibrational mode assignments of the new peaks formed for the boron-containing sample are included in Table 3.

As evident in Figures 4 and 5, the peaks between 2100 and 2300 cm⁻¹ produced by the ν_8 and ν_9 fundamental modes and the $\nu_6 + \nu_7$ combination band of the [DCA]⁻ anion have decreased in amplitude by the factor of approximately 20 following oxidation, which suggests that the [DCA]⁻ anion has essentially been degraded by reaction with the nitrogen dioxide. In contrast, the bands produced by the [BMIM]⁺ cation, for example the structure between 2800 and 3400 cm⁻¹,

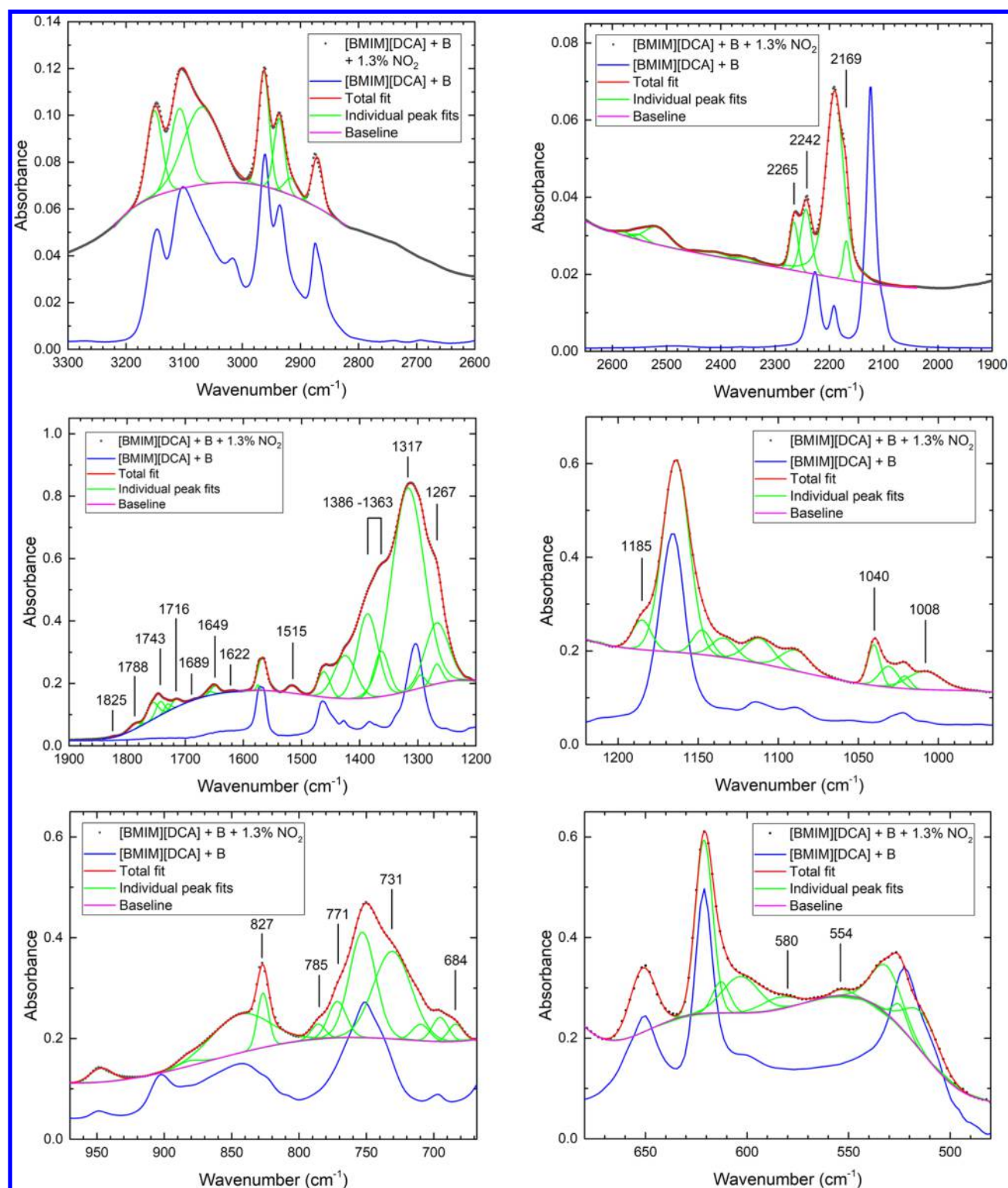


Figure 5. FTIR spectra and individual peak fits of boron-doped [BMIM][DCA] after the oxidation. The spectra of boron-doped [BMIM][DCA] before the reaction are presented for comparison purposes (blue lines). The wavenumbers of the newly formed peaks are identified by the vertical lines and the vibrational assignments are given in Table 3. The unreacted spectrum in the 2650–1900 cm^{-1} region has been scaled by the factor of 0.05.

are almost the same before and after reaction, and therefore the cation must remain mainly intact.

Finally, note that several new peaks occur between 1700 and 1800 cm^{-1} , in particular those at 1716, 1743, and 1788 cm^{-1} . Functional groups of organic nitrogen compounds do not

produce bands with wavenumbers above approximately 1700 cm^{-1} .³⁰ The 1700–1800 cm^{-1} wavenumber region is, however, dominated by absorptions from the stretching modes of the carbonyl functional group ($\text{C}=\text{O}$).³⁰ The new peaks could therefore be produced by a $\text{C}=\text{O}$ functional group that forms

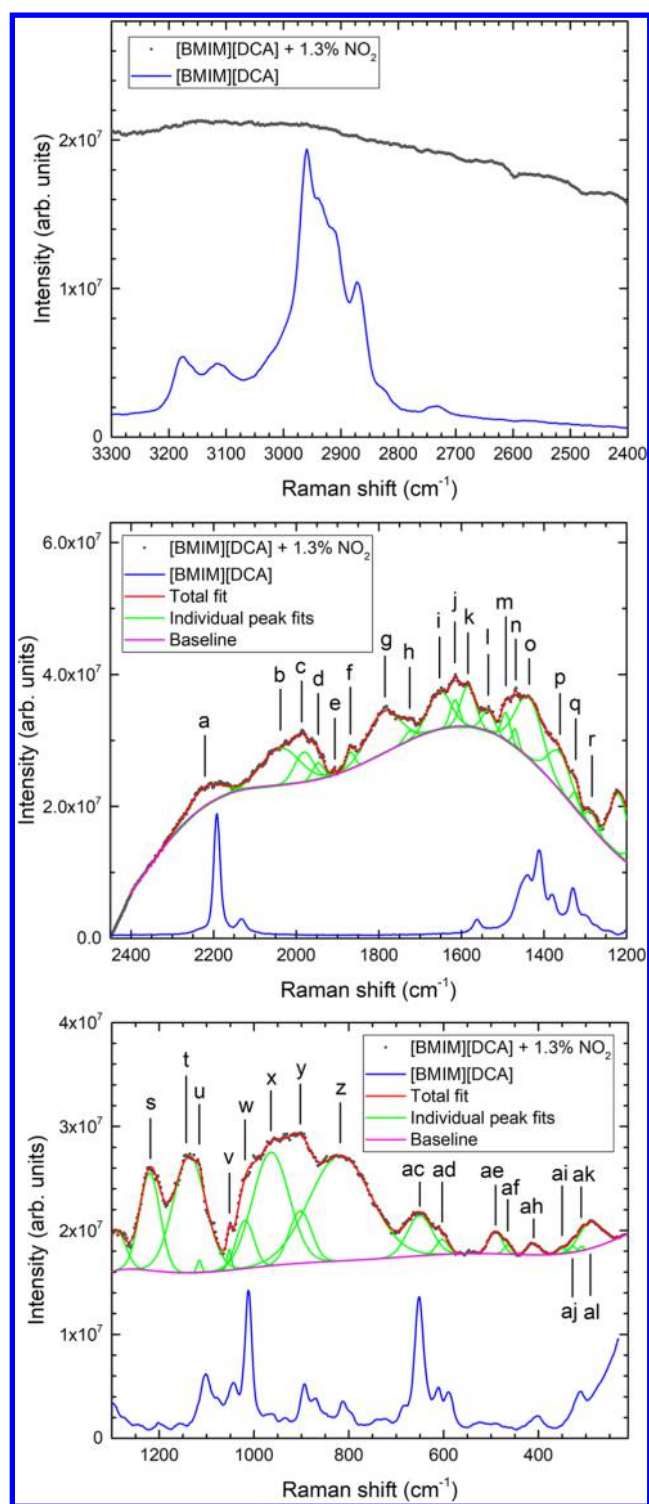


Figure 6. Raman spectra of a levitated [BMIM][DCA] droplet after the oxidation (black circles). Spectra of unreacted [BMIM][DCA] are displayed for comparison purposes (blue lines). In the low Raman-shift region from 2450 to 210 cm^{-1} , the total fit (red line) and individual peak fits (green lines) are shown. The wavenumbers of the newly formed vibrational modes are identified by the vertical lines, and the assignments for the peaks labeled a–al are given in Table 4. A linear background has been removed from the reacted spectra for comparison purposes.

part of molecules produced by higher-order reactions. Alternatively, the new peaks in the 1700–1800 cm^{-1} region

could be caused by dinitrogen tetroxide (N_2O_4) dissolved in the droplet. The possibility of dissolved N_2O_4 is supported by the UV–visible spectra of the same droplet, as discussed in section 3.2.3, which closely resemble the combined spectra of N_2O_4 and NO_2 . Furthermore, the wavenumbers of ν_5 , ν_9 , $\nu_4 + \nu_5$ modes of N_2O_4 at 1712, 1758, and 1791 cm^{-1} are similar to the experimental values.³⁶

3.2.2. Raman Spectroscopy. The Raman spectra of a [BMIM][DCA] droplet levitated in 1.3% NO_2 and 98.7% Ar are shown in Figure 6. The bottom curves in each figure display the spectra before reaction (blue line), whereas the top curves are the spectra produced after reaction with the nitrogen dioxide gas (black circles). In the high Raman-shift region between 3800 and 2400 cm^{-1} , the nitrogen dioxide causes the amplitudes of the peaks for the unreacted [BMIM][DCA] nearly to vanish and a broad, structureless continuum to appear. Similarly, in the low Raman-shift region from 2450 to 300 cm^{-1} , the reaction causes the sharp peaks from the unreacted [BMIM][DCA] to reduce significantly, but here multiple broad, new features appear. The total fit to the new features (red line) and individual peak fits (green lines) are shown in Figure 6 with the wavenumbers of the peaks presented in Table 4.^{30,36–47} Although the fitting procedure is considerably complicated by the series of broad, overlapping new peaks, it is possible to identify the individual bands composing the total spectrum in most wavenumbers regions. The only clear exception occurs in the region between approximately 2150 and 1900 cm^{-1} , where the three fitted peaks are probably better regarded as an unresolved combination of modes from 1950–2040 cm^{-1} .

To assign vibrational modes to the new peaks, we searched for suitable functional groups that are active in the range of the new structure from 2300 to 230 cm^{-1} .³⁰ As for the FTIR spectra, the simplest mechanism to form the new peaks would involve the nitrogen or oxygen atom of the nitrogen dioxide reactant bonding to a carbon or nitrogen atom of [BMIM][DCA]. In Table 4, we therefore list functional groups of organic nitro-compounds with ranges of absorption closest to the measured wavenumbers of the new peaks. Thus, the appearance of the new structure is consistent with formation of the organic nitro-compounds including organic nitrites (RONO), nitroamines ($\text{RR}'\text{NNO}_2$), dinitroalkanes ($\text{RR}'\text{CH}(\text{NO}_2)_2$), carbonitrates ($\text{RR}'\text{C}=\text{NO}_2^-$), aromatic nitro-compounds (ArNO_2), and saturated primary ($\text{H}_2\text{C}=\text{NO}_2$) and secondary aliphatic nitro-compounds ($\text{RR}'\text{CHNO}_2$). However, functional groups of organic nitro-compounds only produce bands in the 1680–475 cm^{-1} region.³⁰ We therefore searched for molecules containing oxygen and nitrogen atoms which are Raman active in the 2300–1700 cm^{-1} and 450–230 cm^{-1} ranges. To select suitable candidates from the large number of possible molecules, moieties were chosen that formed part of the organic nitro-compounds produced by reaction between [BMIM][DCA] and nitrogen dioxide. Unreacted [BMIM][DCA] might contribute to the final reacted spectrum in some wavenumber regions, for example, from 2250 to 2150 cm^{-1} and 1510 to 1260 cm^{-1} where the original molecule produces large peaks (Table 4).

The corresponding Raman spectra for a boron-doped [BMIM][DCA] droplet levitated in the same nitrogen dioxide and argon gas mixture are shown in Figure 7. The total fit to the new structure (red line) and individual peak fits (green lines) are displayed in Figure 7. The best-fit peak wavenumbers are presented in Table 4. As comparison of the unreacted

Table 4. Wavenumbers and assignments of the New Peaks a–l in the Raman Spectra of Pure or Boron-Doped [BMIM][DCA] after Levitation in 1.3% NO₂ and 98.7% Ar (Figures 6 and 7)^a

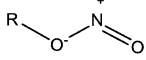
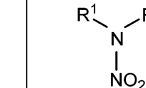
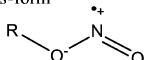
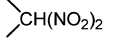
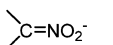
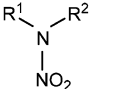
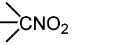
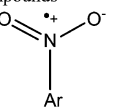
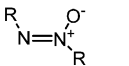
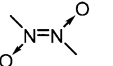
Measured wavenumber [BMIM][DCA] (cm ⁻¹)	Measured wavenumber boron-doped [BMIM][DCA] (cm ⁻¹)	Functional group or molecule	Region* (cm ⁻¹)	Vibrational modes	Ref.
a) 2221 ± 4	a) 2220 ± 10	Unreacted [DCA]	2133 2192 2228	See Table 2	
b) 2038 ± 9	b) 2020 ± 10	N-O-C=N O=C-N=O N=C=O ⁺	2086.0 w 2045.1 2020 ± 30	CN stretch, ν ₁ CO stretch, ν ₁ stretch, ν ₁	37 38 39
c) 1981 ± 5	c) 1986 ± 5	C=N-N=O	1997.5 m 1967.5 m	CN stretch, ν ₁	37
d) 1947 ± 4	d) 1951 ± 3	HNO ⁺ N=C-N=O	1960 ± 30 1956	NO stretch, ν ₃ CN stretch, ν ₁	40 41
e) 1907 ± 3	e) 1905 ± 3	N=C=O	1921.28	asym. stretch, ν ₉	42
f) 1869 ± 1	f) 1868 ± 3	N-O-C=N	1841.1	NO stretch, ν ₂	43
g) 1789 ± 4	g) 1784 ± 6	N ₂ O ₄ N ₂ O ₄	1791 1758	ν ₄ + ν ₅ ν ₉	36 36
h) 1725 ± 2	h) 1722 ± 2	N ₂ O ₄	1712	ν ₅	36
i) 1653 ± 3	i) 1657 ± 4	Organic nitrites, <i>trans</i> -form 	1680 - 1650 vs	N=O str. primary ~ 1675 cm ⁻¹ secondary ~ 1665 cm ⁻¹ tertiary ~ 1625 cm ⁻¹	30
j) 1616 ± 2	j) 1615 ± 4	Nitroamines 	1630 - 1530 s	sym. NO ₂ str.	30
j) 1616 ± 2	j) 1615 ± 4	Organic nitrites, <i>cis</i> -form 	1625 - 1610 vs	N=O str. secondary ~ 1615 cm ⁻¹ tertiary ~ 1610 cm ⁻¹	30
k) 1584 ± 3	k) 1580 ± 3	Dinitroalkanes 	1590 - 1570 m-w	asym. NO ₂ str.	30
k) 1584 ± 3	k) 1580 ± 3	Carbonitrates 	1605 - 1575 s	C=N str.	30
k) 1584 ± 3	k) 1580 ± 3	Saturated aliphatic nitroamines 	1585 - 1530 m-s	asym. NO ₂ str.	30
l) 1535 ± 3	l) 1534 ± 3	Saturated tertiary aliphatic nitro compounds 	1555 - 1530 m-w	asym. NO ₂ str.	30
l) 1535 ± 3	l) 1534 ± 3	Aromatic nitro-compounds 	1580 - 1485 m-w	asym. NO ₂ str.	30
l) 1535 ± 3	l) 1534 ± 3	Saturated aliphatic nitroamines	1585 - 1530 m-s	asym. NO ₂ str.	30
m) 1492 ± 2	m) 1493 ± 2	Aromatic nitro-compounds	1580 - 1485 m-w	asym. NO ₂ str.	30
n) 1470 ± 3	n) 1470 ± 2	Aromatic azoxy compounds 	1480 - 1450 m-s	asym. N=N-O str. Tentative assignment.	30
n) 1470 ± 3	n) 1470 ± 2	Organic nitroso compound <i>Trans</i> -dimers Aromatic compounds 	1480 - 1450 vs	N=N str. Tentative assignment	30

Table 4. continued

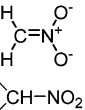
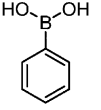
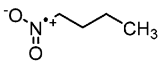
Measured wavenumber [BMIM][DCA] (cm ⁻¹)	Measured wavenumber boron-doped [BMIM][DCA] (cm ⁻¹)	Functional group or molecule	Region* (cm ⁻¹)	Vibrational modes	Ref.
o) 1436 ± 3	o) 1439 ± 2	Primary nitroalkanes 	≈ 1430 m	def. vib. of adjacent methylene group	30
o) 1436 ± 3	o) 1439 ± 2	Unreacted [BMIM][DCA]	1445 1438 1411	Table 2	
-	o) 1439 ± 2	B-N	1465 - 1330 m	B-N str.	30
p) 1361 ± 5	p) 1360 ± 2	Saturated primary and secondary aliphatic nitro-compounds 	1385-1360 s	sym. NO ₂ str., CH ₂ def. vib.	30
p) 1361 ± 5	p) 1360 ± 2	Dinitroalkanes	1375 - 1340 s	sym. NO ₂ str.	30
p) 1361 ± 5	p) 1360 ± 2	Aromatic nitro-compounds	1370 - 1315 s	sym. NO ₂ str.	30
p) 1361 ± 5	p) 1360 ± 2	Unreacted [BMIM][DCA]	1381	Table 2	
q) 1323 ± 1	q) 1322 ± 2	Aromatic nitro-compounds	1370 - 1315 s	sym. NO ₂ str.	30
q) 1323 ± 1	q) 1322 ± 2	Unreacted [BMIM][DCA]	1329	Table 2	
r) 1284 ± 2	r) 1286 ± 2	Nitroamines	1315 - 1260 v, p	sym. NO ₂ str.	30
r) 1284 ± 2	r) 1286 ± 2	Carbonitrates	1315 - 1205 m-w	asym. NO ₂ str.	30
r) 1284 ± 2	r) 1286 ± 2	Unreacted [BMIM][DCA]	1299	Table 2	
s) 1218 ± 1	s) 1218 ± 1	o-Aminonitro-aromatic compounds	1260 - 1215 s	sym. NO ₂ str. Tentative assignment	30
s) 1218 ± 1	s) 1218 ± 1	Carbonitrates	1315 - 1205 m-w	asym. NO ₂ str.	30
t) 1138 ± 1	t) 1141 ± 1	Aromatic nitro-compounds	1180 - 865 m-s	CN str.	30
t) 1138 ± 1	t) 1141 ± 1	Carbonitrates	1175 - 1040 s	sym. NO ₂ str.	30
u) 1115 ± 2	u) 1116 ± 1	Aromatic nitro-compounds	1180 - 865 m-s	CN str.	30
u) 1115 ± 2	u) 1116 ± 1	Carbonitrates	1175- 1040 s	sym. NO ₂ str.	30
v) 1052 ± 1	v) 1056 ± 2	Aromatic nitro compounds	1180 - 865 m-s	CN str.	30
v) 1052 ± 1	v) 1056 ± 2	Carbonitrates	1175 - 1040 s	sym. NO ₂ str.	30
v) 1052 ± 1	v) 1056 ± 2	Unreacted [BMIM][DCA]	1044	See Table 2	
w) 1019 ± 2	w) 1012 ± 5	Aromatic nitro-compounds	1180 - 865 m-s	CN str.	30
w) 1019 ± 2	w) 1012 ± 5	Nitroamines	1030 - 980 s, p	N-N str.	30
w) 1019 ± 2	w) 1012 ± 5	Unreacted [BMIM][DCA]	1011	Table 2	
x) 964 ± 3	x) 969 ± 5	Saturated primary and secondary aliphatic nitro-compounds	1000 - 915 m-s, p	C-N str., <i>trans</i> -form	30
x) 964 ± 3	x) 969 ± 5	Aromatic nitro-compounds	1180 - 865 m-s	CN str.	30
y) 903 ± 6	y) 921 ± 5	Saturated primary and secondary aliphatic nitro-compounds	920 - 850 m-s, p	br., C- N str., <i>gauche</i> -form	30
y) 903 ± 6	y) 921 ± 5	Aromatic nitro compounds	1180 - 865 m-s	CN str.	30
y) 903 ± 6	y) 921 ± 5	Unreacted [BMIM][DCA]	894 871	Table 2	
z) 820 ± 10	z) 815 ± 7	Nitrites, <i>cis</i> -form	850 - 810 m	N-O str.	30

Table 4. continued

Measured wavenumber [BMIM][DCA] (cm ⁻¹)	Measured wavenumber boron-doped [BMIM][DCA] (cm ⁻¹)	Functional group or molecule	Region* (cm ⁻¹)	Vibrational modes	Ref.
	aa) 732 ± 2	B-OH, aryl boronic acids 	800 - 700		30
	ab) 686 ± 4	Nitrites, <i>cis</i> -form	690 - 615	O-N=O def. vib.	30
ac) 650 ± 2	ac) 653 ± 5	Saturated primary and secondary aliphatic nitro-compounds	655 - 605 m, p	NO ₂ def. vib.	30
ac) 650 ± 2	ac) 653 ± 5	Nitroamines	730 - 590 m	NO ₂ wagging vib.	30
ac) 650 ± 2	ac) 653 ± 5	Unreacted [BMIM][DCA]	652	Table 2	
ad) 603 ± 2	ad) 611 ± 2	Straight-chain primary nitroalkanes 	620 - 600 m-w	sym. NO ₂ def. vib.	30
ad) 603 ± 2	ad) 611 ± 2	Nitroamines	730 - 590 m	NO ₂ wagging vib.	30
ad) 603 ± 2	ad) 611 ± 2	Nitroamines	620 - 560 v	NO ₂ rocking vib.	30
ad) 603 ± 2	ad) 611 ± 2	Unreacted [BMIM][DCA]	611 589	aj ak	Table 2
ae) 491 ± 3	ae) 504 ± 3	Saturated primary and secondary aliphatic nitro-compounds	560 - 470 v	NO ₂ rocking vib.	30
af) 465 ± 4	af) 477 ± 4	straight-chain primary nitroalkanes	490 - 465 m-w	NO ₂ rocking vib.	30
-	ag) 438 ± 3	H ₂ N-NO ₂	418	torsion, ν ₁₂	44
ah) 410 ± 2	ah) 419 ± 4	N ₂ O ₄	425	ν ₇	36
ah) 410 ± 2	ah) 419 ± 4	N=C-N=O	411	torsion, ν ₆	41
ah) 410 ± 2	ah) 419 ± 4	Unreacted [BMIM][DCA]	426 ± 9 402 ± 2	Table 2	
ah) 410 ± 2	ah) 419 ± 4	H ₂ N-NO ₂	402	torsion, ν ₁₂	44
ai) 350 ± 10	-	H-C=N-O	345 ± 5	bend	45
aj) 328 ± 6	-	Unreacted [BMIM][DCA]	325 ± 13	Table 2	
ak) 310 ± 5	ak) 306 ± 1	Unreacted [BMIM][DCA]	312	Table 2	
ak) 310 ± 5	ak) 306 ± 1	ONO-NO ₂ (D)	306.0	O-N stretch, ν ₈	46
al) 291 ± 4	-	ONO-NO ₂ (D)	306.0	O-N stretch, ν ₈	46
al) 291 ± 4	-	N ₂ O ₄	~270	ν ₁₀	36
al) 291 ± 4	-	N=C-N=O	264.2	torsion, ν ₆	47
al) 291 ± 4	-	C=N-N=O	261.0 m-s	NN stretch, ν ₄	37

^aThe assignments in the 1700–450 cm⁻¹ range were performed by comparison with the regions of maximum absorption, Raman intensities, and vibrational modes of the functional groups tabulated in ref 30. The vibrational energy levels from refs 36–47 were used to assign the remaining spectral regions. *Key: v = very strong, s = strong, m = medium, w = weak, p = polarized.

spectra in Figures 6 and 7 (blue lines) shows, adding the boron nanoparticles to [BMIM][DCA] causes the sharp peaks to vanish and a large structureless continuum to appear. Similar spectra with broad continua and an absence of sharp features are characteristic of the Raman spectra of amorphous boron.⁴⁸ The large reduction in the [BMIM][DCA] peaks is also a consequence of absorption of the 532 nm laser beam by the boron nanoparticles, which results in a significantly reduced path length of the ionic liquid sampled. Although the unreacted pure and boron-doped samples produce distinct spectra, following reaction with nitrogen dioxide the resulting spectra are almost identical with or without the boron nanoparticles. Consequently, the same reaction products must form on the surface of the droplet as for the pure [BMIM][DCA] sample. Furthermore, the Raman activity of the newly formed molecules must be high to dominate the initial contribution from the boron nanoparticles. As for the FTIR data discussed in section 3.2, the formation of most of

the new peaks can therefore be explained by the nitrogen dioxide molecule bonding to [BMIM][DCA] to form nitro-compounds instead of an initial reaction of nitrogen dioxide with the boron-based nanoparticles. There are, however, a few small but significant differences between the spectra with or without the boron nanoparticles. First, the broad peak at around 1440 cm⁻¹ is more prominent for the boron-containing sample, which could be caused by a contribution from the B–N stretching mode (Table 4).³⁰ Second, a very small peak at 732 cm⁻¹, which could be produced by the B–OH functional group of boronic acid,³⁰ is present only for the boron-containing sample.

3.2.3. UV–Visible Spectroscopy. We employed *in situ* UV–visible reflectance spectroscopy in the 200–1100 nm wavelength range to provide further information about the oxidation of pure or boron-doped [BMIM][DCA] droplets. First, the spectra before the reaction with the nitrogen dioxide gas are discussed. As shown in Figure 8a (black line), there is a

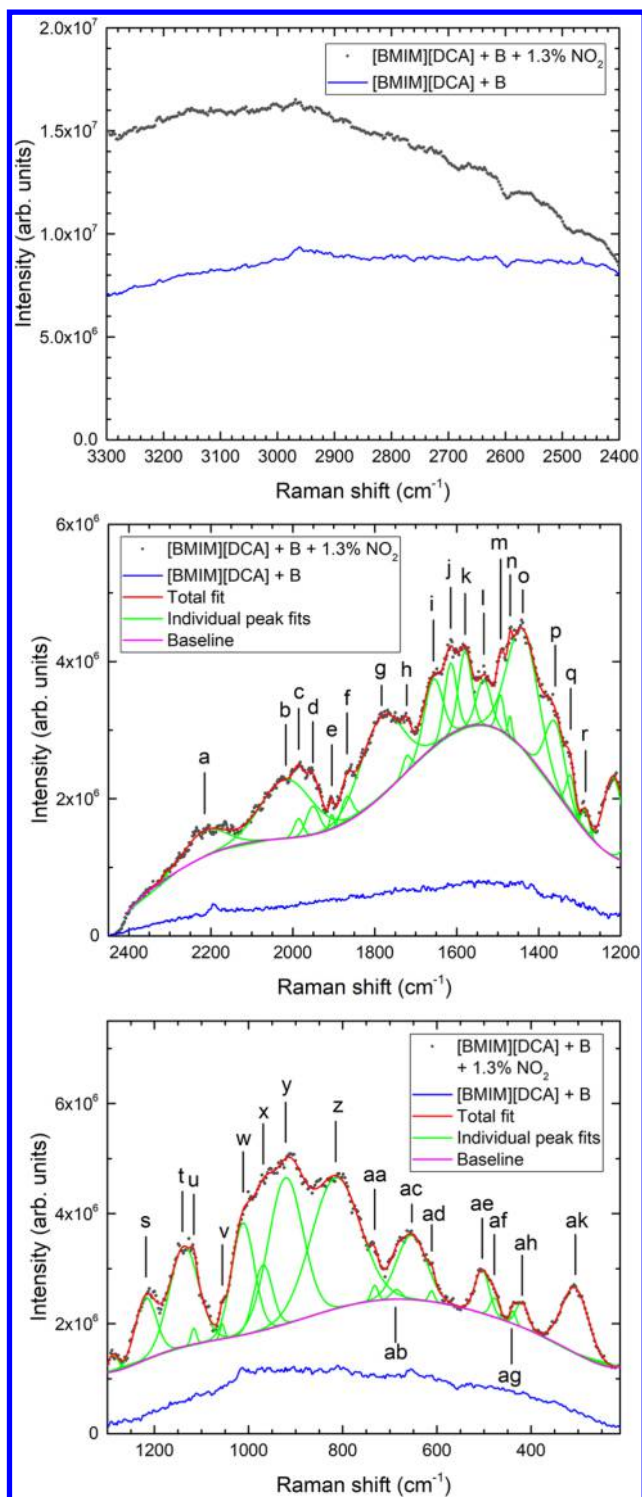


Figure 7. Raman spectra of a levitated, boron-doped [BMIM][DCA] droplet after oxidation (black circles). Spectra of nonreacted, boron-doped [BMIM][DCA] are displayed for comparison purposes (blue lines). In the low Raman-shift region from 2450 to 210 cm^{-1} , the total fit (red line) and individual peak fits (green lines) are shown. The wavenumbers of the newly formed vibrational modes are identified by the vertical lines, and the assignments for the peaks labeled a–ak are given in Table 4. A linear background has been removed from the reacted spectra for comparison purposes.

minimum in the reflectance of [BMIM][DCA] or a maximum in the absorption from approximately 220 to 310 nm. The

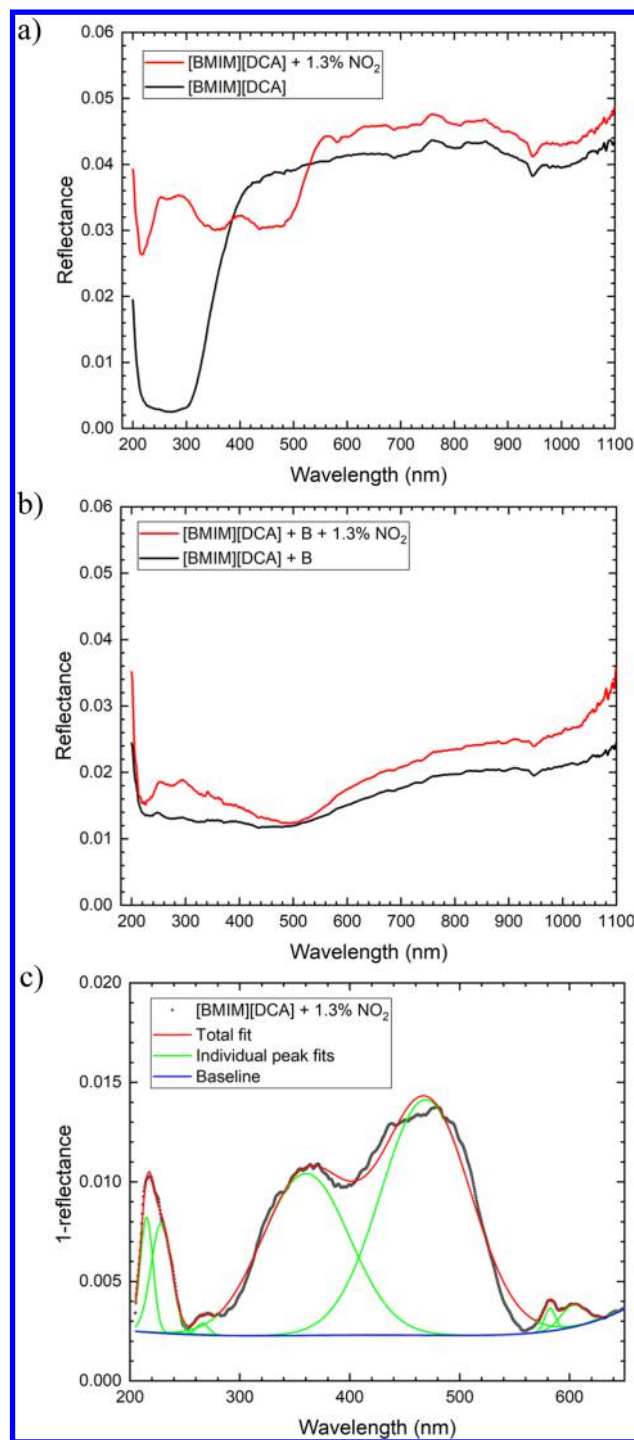


Figure 8. UV–visible reflectance spectra for a levitated droplet of (a) [BMIM][DCA] and (b) [BMIM][DCA] doped with hydrogen-capped boron nanoparticles. Reference spectra collected before the reaction (black lines) are compared with the spectra after reaction with the nitrogen dioxide (red lines). (c) Fits to the absorption peaks of the reacted [BMIM][DCA] in the 200–650 nm region (a linear background has been subtracted).

reflectance of [BMIM][DCA] was placed on an absolute scale by substituting the value for the refractive index of [BMIM]-[DCA] at 589 nm (sodium D-line)⁴⁹ ($n_D(589 \text{ nm}) = 1.50890 \pm 0.00004$) into the Fresnel equation at normal incidence. The resulting value for the reflectance of [BMIM][DCA] at 589 nm is 0.0411. The correction factor so obtained to convert the

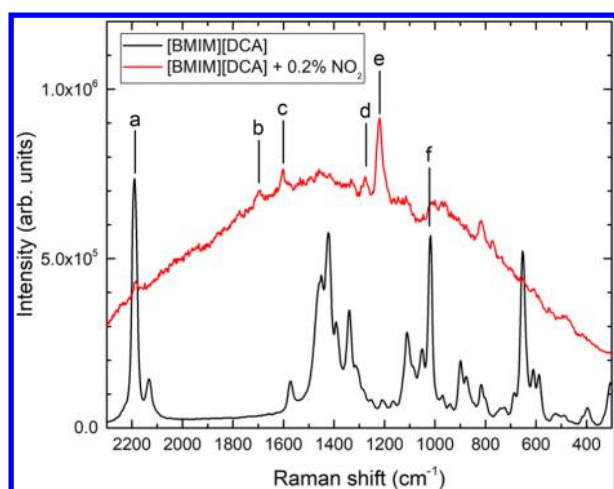


Figure 9. Bottom curve (black line) and the top curve (red line) display the Raman spectra of a levitated [BMIM][DCA] droplet before and after oxidation, respectively. The peaks labeled (a) and (f) are present in unreacted [BMIM][DCA], whereas peaks b–e are new and form because of oxidation by the nitrogen dioxide.

observed reflected intensity to the absolute reflectance was applied to the other reflectance spectra presented here. However, owing to changes in the dimensions, shape, and position of the droplet during the reactions, for example, such as occurs when a bubble forms inside the droplet (Figure 1), the absolute reflectance scale for samples other than pure [BMIM][DCA] is only approximate. The ionic liquid blackens when the boron nanoparticles are added. Therefore, as comparison of the unreacted spectra in Figure 8a, b (black lines) shows, the region of high absorption previously from 220 to 310 nm extends across the full wavelength range. The absorption of electromagnetic radiation from 200 to 1100 nm is the result of interband transitions in the boron nanoparticles.^{50,51}

As shown in Figure 8a, because of interaction with the nitrogen dioxide at a concentration of 1.3%, the reflectance spectrum of [BMIM][DCA] developed several new minima in the 200–650 nm range. To help visualize and identify the corresponding new *absorption* structures, in Figure 8c we present fits to the spectrum of $1 - \text{reflectance} (R)$ in the 200–650 nm region. The resulting peaks, although related to the absorption, A , of the processed ionic liquid, cannot be placed on an absolute scale, since $A = 1 - R - T$ and the transmittance, T , cannot be measured with the present experimental set up. The fits reveal that a relatively sharp absorption peak appears at 215 nm; two very broad structures

are produced with maxima at approximately 350 and 470 nm; and three new smaller peaks occur at 269, 579, and 607 nm. As evident in Figure 8b, the new structure produced by the nitrogen dioxide is less prominent for the boron-containing sample. The two minima in the reflectance at around 220 and 270 nm can also be discerned in Figure 8b, but only one very broad reflectance minimum appears from approximately 300 to 700 nm.

In Figure 8c, the relatively sharp peak at 215 nm and the broad absorption structure with a maximum at around 470 nm resemble the absorption spectrum of nitrogen dioxide in the same spectral range.⁵² Furthermore, the broad peak with a maximum near 350 nm is similar to the peak in the absorption spectrum of dinitrogen tetroxide (N_2O_4) in the 180–390 nm wavelength range.⁵³ Therefore, the largest structures in Figure 8c could have formed by nitrogen dioxide and dinitrogen tetroxide dissolving in the droplet. The contribution of unreacted [BMIM][DCA] to the spectra of the processed droplet in Figure 8a or Figure 8c appears to be small, whereas the absorption structure of the newly formed or introduced molecules dominates. Therefore, the nitrogen dioxide and dinitrogen tetroxide would need to have a relatively high concentration near the surface of the droplet where the detection sensitivity of the UV–visible probe is highest. Dissolved dinitrogen tetroxide in the droplet is consistent with the analysis of the FTIR and Raman spectra of [BMIM][DCA] after reaction with nitrogen dioxide (section 3.2), where new features at several wavenumbers possibly could be explained by vibrational modes of the dinitrogen tetroxide molecule (Tables 3 and 4).

3.3. Reaction Rates. In addition to identifying the newly emerging bands, we also extracted reaction rates for the oxidation of the pure and boron-doped [BMIM][DCA] and [MAT][DCA] droplets by nitrogen dioxide. We consider the decay of the peaks associated with the anion and cation of the unreacted ionic liquid and also the formation of the newly emerging peaks produced by the oxidation. It is important to highlight that, when levitating a droplet, there is a minimum time delay of approximately 20 s between when the liquid first appears on the end of the needle and completing collection of the Raman spectrum. At nitrogen dioxide concentrations of 1.3%, the heights of the broad peaks in the Raman spectra (section 3.2.2) reached their final values within 20 s and, hence, it is not feasible to determine the corresponding rates of formation with the present experimental set up. However, when the concentration of the nitrogen dioxide is reduced from 1.3% to 0.2%, the relatively sharp peaks b–e shown in Figure 9 appear in place of the broad structure. The formation

Table 5. Wavenumbers and Assignments of Vibrational Modes for the New Peaks Formed in the Raman Spectra of Pure or Boron-Doped [BMIM][DCA] Droplets When Levitated in 0.2% NO_2 and 99.8% Ar ^a

peak	wavenumber [BMIM][DCA] (cm^{-1})	wavenumber boron-doped [BMIM][DCA] (cm^{-1})	functional group	region (cm^{-1})	Raman intensity ^b	vibrational mode
b	1698 ± 2	1699 ± 1	organic nitrites, <i>trans</i> -form	1650–1680	s	N=O str. Primary $\sim 1675 \text{ cm}^{-1}$
c	1603 ± 1	1600 ± 1	organic nitrites, <i>cis</i> -form	1610–1625	s	N=O str.
d	1275 ± 2	1275 ± 2	nitroamines	1260–1315	v, p	sym. NO_2 str.
e	1219 ± 1	1220 ± 1	nitro-aromatic compounds	1215–1260	s	sym. NO_2 str.

^aThe peak wavenumbers are from the present measurements, whereas the functional groups, regions of maximum absorption, Raman intensities, and vibrational modes are from ref 30. ^bKey: v = very strong, s = strong, m = medium, w = weak, p = polarized.

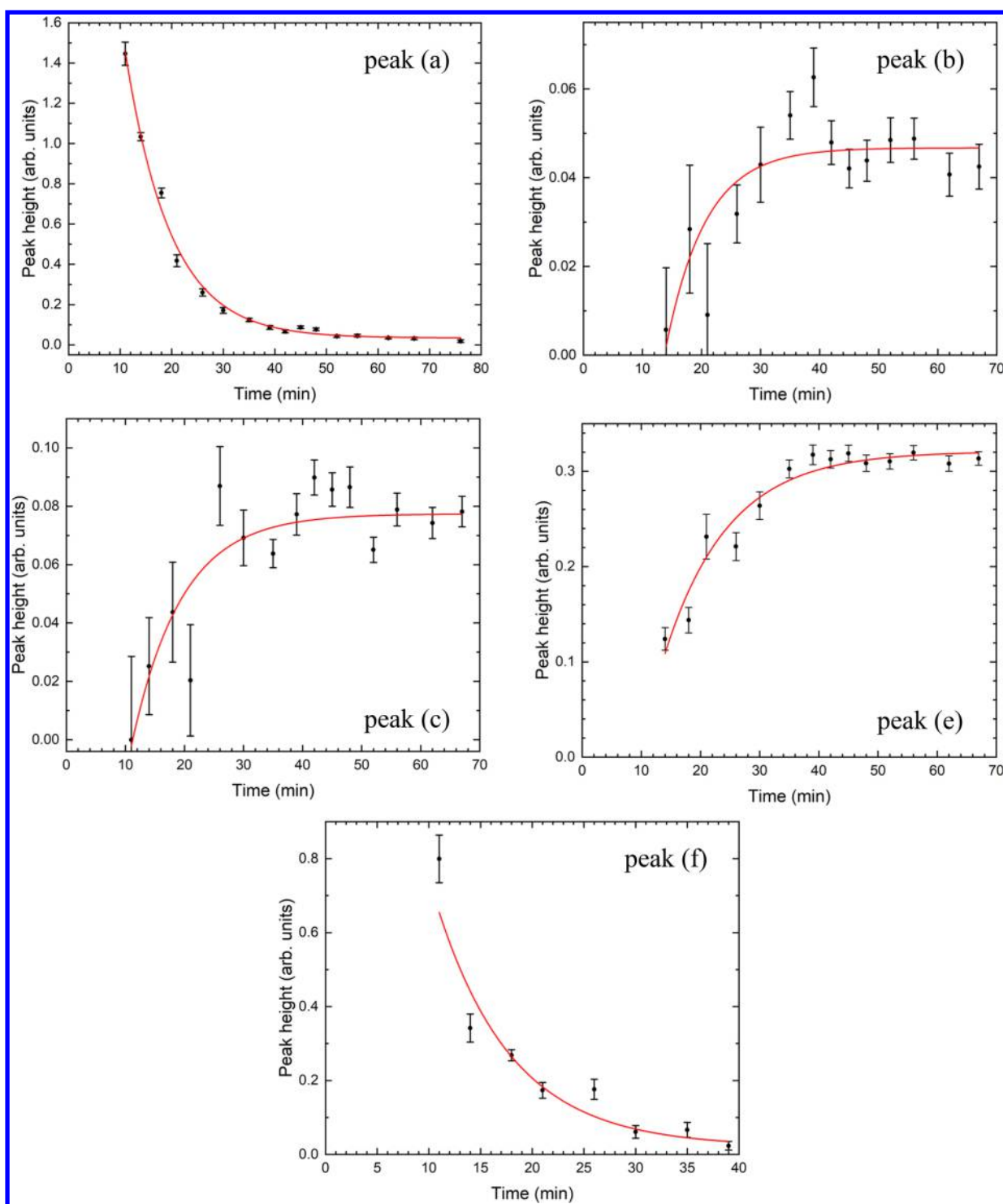


Figure 10. Fits to the decay or rise of peaks a, b, c, e, and f in Figure 9 for a [BMIM][DCA] droplet levitated in 0.2% NO₂ and 99.8% Ar.

of peaks b–e can be traced on timescales of up to 120 min, thus permitting a study of the corresponding reaction rates and, therefore, of the decomposition of the ILs. In Figure 9, the newly emerged peaks b–e are compared with the unreacted [BMIM][DCA] spectrum. The peaks labeled a and f in Figure 9 are present in the unreacted [BMIM][DCA] and correspond to the ν_9 mode of [DCA][−] and the imidazolium ring mode γ of [BMIM]⁺ (section 3.1.2; Table 2), respectively; these modes were selected to investigate possible differences in reactivity for the [BMIM]⁺ cation and the [DCA][−] anion. Following the

same procedure as discussed in section 3.2, the vibrational modes and functional groups of the new peaks b to e are assigned in Table 5.³⁰ The peaks at 1603 and 1698 cm^{−1} could be accounted for by the N=O stretching modes of the *cis*- and *trans*-forms of the organic nitrites (RONO), respectively. The smaller peak at 1275 cm^{−1} might be attributed to a symmetric NO₂ stretching mode of the nitroamines (RR'NNO₂). Finally, the largest peak at 1219 cm^{−1} occurs in the wavenumber range of the symmetric NO₂ stretching modes of the aromatic nitro-compounds (ArNO₂). The wavenumber range for the nitro-

Table 6. Time Delays, Δt , and Reaction Rates, k , for the Formation or Decay of Peaks a–f in the Raman Spectra of Pure or Boron-Doped [BMIM][DCA] Droplets When Levitated in 0.2% NO_2 and 99.8% Ar ^a

peak	no boron		with boron	
	time delay Δt (min)	reaction rate k (10^{-3} s^{-1})	time delay Δt (min)	reaction rate k (10^{-4} s^{-1})
a		1.90 ± 0.10		7.74 ± 0.52
b	14 ± 12	2.5 ± 1.4	16.7 ± 3.7	10.5 ± 1.4
c	11.2 ± 9.9	2.0 ± 1.0	13.1 ± 3.7	6.69 ± 0.97
d			20.0 ± 6.4	9.8 ± 2.0
e	9.5 ± 3.2	1.54 ± 0.27	14.2 ± 1.5	8.53 ± 0.53
f		2.28 ± 0.57		

^aParameters are unavailable for two of the peaks for reasons explained in the text.

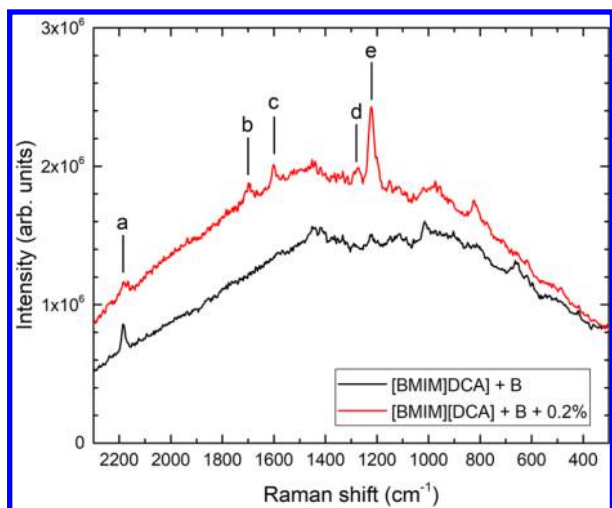


Figure 11. Bottom curve (black line) and the top curve (red line) are the Raman spectra of a boron-doped [BMIM][DCA] droplet before and after levitating in 0.2% NO_2 and 99.8% Ar , respectively. The peak labeled (a) is present in unreacted boron-doped [BMIM][DCA], whereas peaks b–e are new and form because of reaction with the nitrogen dioxide.

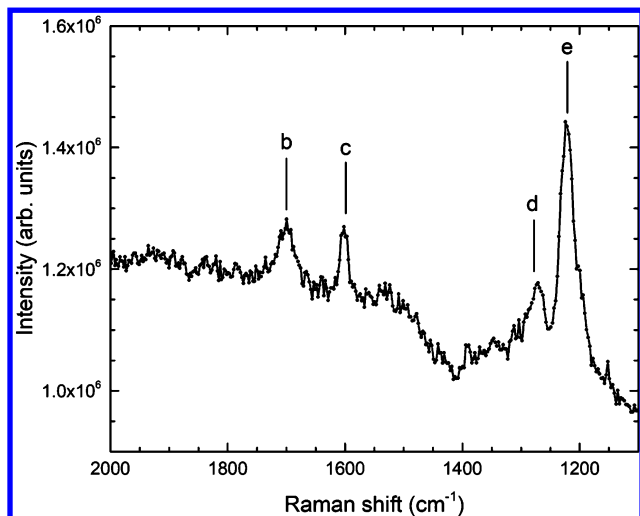


Figure 12. Difference between the Raman spectra of a boron-doped [BMIM][DCA] droplet before and after levitating in 0.2% NO_2 and 99.8% Ar (see Figure 11) to emphasize the newly formed peaks.

aromatic compounds from 1215 to 1370 cm^{-1} includes the possible effects of strong *o*- or *p*-electron donors, which can shift the absorption region to lower wavenumbers.³⁰ These findings suggest that the nitrogen dioxide oxidizes the [BMIM][DCA] through bond formation via carbon–oxygen linkages for absorptions b and c and nitrogen–nitrogen linkages for peak d. Furthermore, the formation of peak e, which is possibly produced by an aromatic nitro-compound, requires the nitrogen atom of the nitrogen dioxide molecule to bond with the 6π imidazolium ring ($\text{C}_3\text{N}_2\text{H}_3$); since nitrogen cannot be pentavalent, the nitrogen–nitrogen bond must be formed at the N(3) atom holding the methyl group (Schemes 1 and 2).

Raman spectra were recorded from the beginning to the completion of the oxidation process, so that the decrease in the heights of peaks a and f and the increase in the heights of peaks b to e could be traced as a function of time. The resulting decay and growth curves are compiled in Figure 10. Since peaks b–d are small and appear superimposed upon a significant background, it is only possible to obtain their heights with accuracy after the initial stages of the reactions and, hence, some of the growth curves have no data points at the beginning of the reactions. We found that the time-dependent curves are well-described by a first-order exponential decay or rise formula. Clearly, there is an initial time period, Δt , when the peak areas did not change significantly, after which the time-dependent curves begin the usual exponential rise, $1 - e^{-k(t-\Delta t)}$, or decay, $e^{-k(t-\Delta t)}$, where k is the reaction rate. The time delay, Δt , is likely a consequence of reactions occurring mainly near the surface of the droplet. Consequently, there is a delay in the increase in the concentration of the product molecules because of the time required for the less reacted ionic liquid in the central regions of the droplet to diffuse to the surface. The time delay is included in Table 6 and was determined by using the fitted parameters for the growth curves to calculate the time when the peak height would have been zero. As an example of a time delay, see curve c in Figure 10 for which the time delay is around 10 min. The time delay cannot be calculated for the decay curves using the fitted parameters, since the effect of a Δt here is to multiply the overall curve by a scale factor, c , that cannot be determined ($e^{-k(t-\Delta t)} = ce^{-kt}$). Table 6 shows that the reaction rates lie within the range of $(1.5\text{--}2.5) \times 10^{-3} \text{ s}^{-1}$. The reaction rate for peak d is not included in Table 6, since it could not be calculated with satisfactory accuracy because of structure from unreacted [BMIM][DCA] present in the same wavenumber region at early stages of the reactions (Figure 9). After accounting for the experimental uncertainties, it is not possible to discern clear, statistically significant differences between the reaction rates of the peaks in Figure 9. Thus, the results are consistent with the different functional groups corresponding to the new peaks b, c, and e forming at the same rate, peaks a and f associated with the unreacted ionic liquid decaying at the same rate as the new peaks appear, and the cation (peak a) and anion (peak f) being equally degraded by the oxidation. The comparable decay and formation rates for all peaks considered suggest a first-order reaction mechanism.

We next determine the effect on the reaction rate of adding hydrogen-capped boron nanoparticles to the [BMIM][DCA] droplet. In Figure 11, the Raman spectra are compared after levitating a droplet in 0.2% NO_2 and 99.8% Ar for 3 and 121 min. The same peaks a–e appear or decay as for the pure [BMIM][DCA] sample, although the imidazolium ring mode y

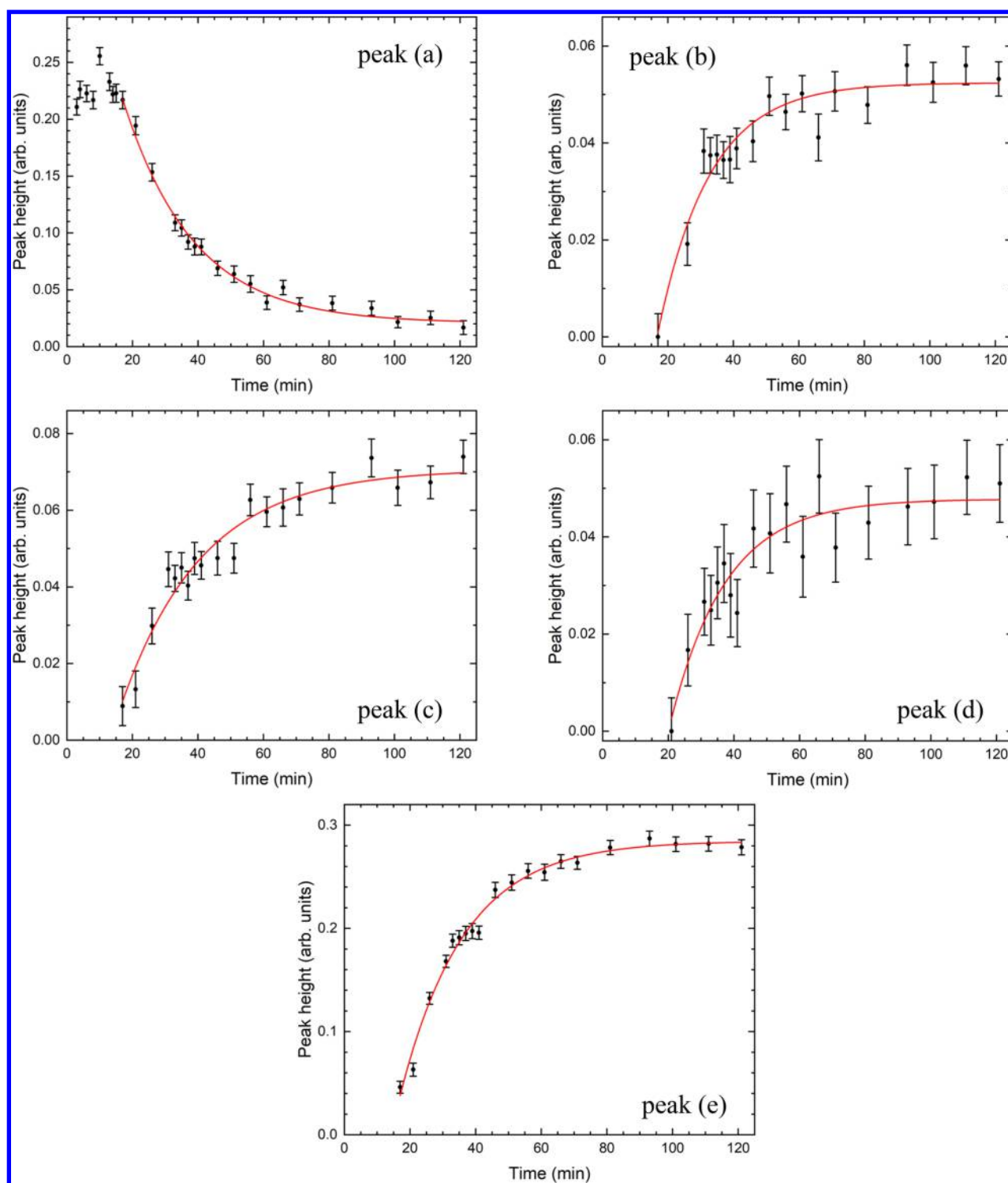


Figure 13. Fits to the decay or rise of peaks a–e in Figure 11 for a boron-doped [BMIM][DCA] droplet levitated in 0.2% NO₂ and 99.8% Ar.

corresponding to peak f cannot be observed because of the large background produced by the boron. To display the newly formed peaks with improved clarity, in Figure 12 the difference is shown between the Raman spectra at 121 and 3 min. The measured wavenumbers and possible vibrational mode assignments for peaks a–e are given in Table 5. The decay and growth curves for peaks a–e are shown in Figure 13. The time delays and reaction rates obtained by fitting first-order exponential decay or rise formulae to the time-dependent curves are presented in Table 6. The reaction rates range from

$(6.7\text{--}10.5) \times 10^{-4} \text{ s}^{-1}$. After accounting for the experimental uncertainties, the results are consistent with a single reaction rate for largest peaks a and e and also for the smaller peak d. The reaction rate for the very small peak c is slightly lower than the other values because of a systematic error produced by the presence of unreacted [BMIM][DCA] at early times. Table 6 reveals that the nanoparticles slow the reaction rate by a factor of approximately 2.4 when averaged over the same peaks. [BMIM][DCA] is known to bind to the surface of boron nanoparticles to form a monolayer with a thickness of

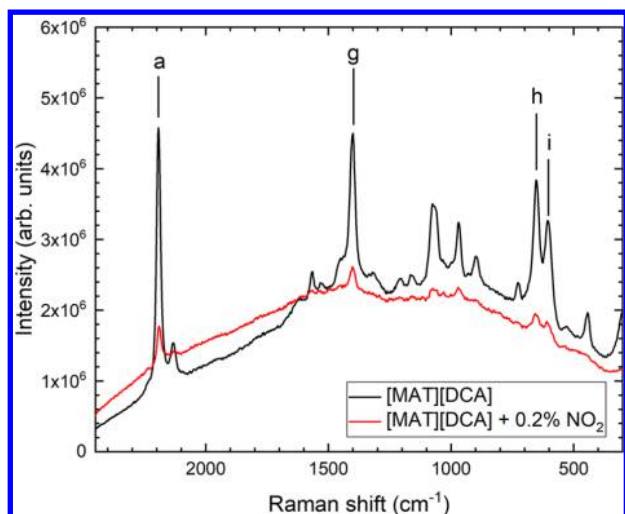


Figure 14. Raman spectra of an [MAT][DCA] droplet before (black line) and after (red line) levitation in 0.2% NO₂ and 99.8% Ar, respectively. The peaks labeled (a), (g), (h), and (i) are present in unreacted [MAT][DCA] and are assigned in Table 7.

approximately 1 nm.²⁰ The interaction of the [BMIM][DCA] with the boron reduces the availability of suitable sites where the nitrogen dioxide can bond with the ionic liquid and, hence, the reaction rate is potentially reduced. However, for boron nanoparticles with typical diameters of 20 nm²⁰ at a concentration of 5% (by weight), less than 1% of the [BMIM][DCA] from the droplet is required to fully coat the surfaces, where 1.06 g cm⁻³ has been used for the density of the IL.⁴⁹ Thus, chemical interactions between the ionic liquid and the homogeneously distributed boron nanoparticles cannot explain the reduced reaction rate. The slower reaction rate could be caused by the increase in the viscosity of a liquid that is known to accompany the introduction of a suspension of small particles.⁵⁴ By increasing the viscosity of the droplet, the boron nanoparticles slow the rate at which the less reacted ionic liquid in the central regions of the droplet diffuses to the surface, reduce the diffusion of the oxidizer into the droplet, hinder the escape of gaseous reaction products from within the droplet, and consequently lower the reaction rate.

Finally, in Figure 14 the Raman spectra of an [MAT][DCA] droplet are compared after levitating in 0.2% NO₂ and 99.8% Ar for 1 and 343 min. For [MAT][DCA], in contrast to [BMIM][DCA], sharp new peaks formed by reaction with 0.2% NO₂ are not observed, and so we can only study the reduction in the amplitudes of peaks produced by the unreacted ionic liquid. The peaks labeled a, g, h, and i in Figure 14 were selected for study because of their large amplitudes and to investigate possible differences in the reaction rates between the [DCA]⁻ anion and [MAT]⁺ cation. The peak wavenumbers and vibrational mode assignments⁵ for the selected peaks of [MAT][DCA] are given in Table 7. The

decay curves for peaks a, g, h, and i are presented in Figure 15, and the reaction rates, obtained by fitting a first-order exponential decay formula to the time-dependent curves, are included in Table 7. Systematic (or nonrandom) errors produced by changes in the droplet size, shape, and position during the measurements are evident in the data. *The reaction rates range from $(7.3 - 10.4) \times 10^{-5} \text{ s}^{-1}$ and so are a factor of approximately 20 lower than for the pure [BMIM][DCA] when averaged over the different peaks.* For the slower reaction rates of [MAT][DCA] compared to [BMIM][DCA], time delays of around 10 min (Table 6) are not apparent in the fitted curves and, hence, are not presented.

4. CONCLUSION

We have extended our previous studies on the oxidation of levitated droplets of [MAT][DCA] and [MAT][DCA] doped with hydrogen-capped boron nanoparticles by nitrogen dioxide in an argon atmosphere.⁵ The experiments utilize an ultrasonic levitator enclosed within a pressure-compatible process chamber equipped with complementary Raman, UV-visible, and FTIR spectroscopic probes. We first analyzed the FTIR spectra of pure and boron-doped [BMIM][DCA] before reaction with nitrogen dioxide. To assign vibrational modes to the peaks in the experimental spectra, the fitted wavenumbers were compared with measured and theoretical values for similar ionic liquids.²⁷⁻²⁹ The FTIR spectra with and without the boron nanoparticles are very similar, except for a small absorption peak at 2490 cm⁻¹ assigned to the $\nu(\text{B-H})$ stretching mode. The peaks in the Raman spectrum of a [BMIM][DCA] droplet levitated in argon were assigned by an analogous procedure.

After levitating a droplet in 1.3% NO₂ and 98.7% Ar, the reaction between the [BMIM][DCA] and the nitrogen dioxide produced numerous new peaks in the FTIR spectra. The simplest mechanism to explain the new structure would involve the nitrogen or oxygen atom of the nitrogen dioxide reactant bonding to a carbon or nitrogen atom of [BMIM][DCA]. We therefore listed functional groups of organic nitro-compounds with ranges of absorption that include the measured wavenumbers of the new peaks, namely, the organic nitrites, nitroamines, aromatic nitro-compounds, and carbonitrates. Several new peaks occur between 1700 and 1800 cm⁻¹, which is outside the wavenumber range of the bands produced by organic nitrogen compounds. The new peaks in the 1700 and 1800 cm⁻¹ region could be produced by carbonyl functional groups (C=O) that form part of molecules produced by higher-order reactions or possibly N₂O₄ dissolved in the droplet. The oxidizer gas produced essentially the same new structure with the boron-doped [BMIM][DCA], and so the formation of the new peaks can also be explained by the nitrogen dioxide molecule bonding to the [BMIM][DCA] rather the boron.

Table 7. Wavenumbers, Vibrational Mode Assignments,⁵ and Reaction Rates k Corresponding to Peaks a, g, h, and i in the Raman Spectra of an [MAT][DCA] Droplet When Levitated in 0.2% NO₂ and 99.8% Ar

peak	wavenumber (cm ⁻¹)	anion or cation	number	vibrational mode	reaction rate k (10^{-5} s^{-1})
a	2193 ± 1	[DCA] ⁻	ν_9	$\nu_s(\text{C}\equiv\text{N}) (A_1)$	10.37 ± 0.62
g	1402 ± 1	[MAT] ⁺	ν_{37}	CH ₂ wag	8.24 ± 0.70
h	652 ± 1	[DCA] ⁻	ν_5	$\delta(\text{CNC}) (A_1)$	8.16 ± 0.73
i	603 ± 1	[MAT] ⁺	ν_{17}	symmetric N-NH ₂ and N-CH ₃ stretch	7.34 ± 0.65

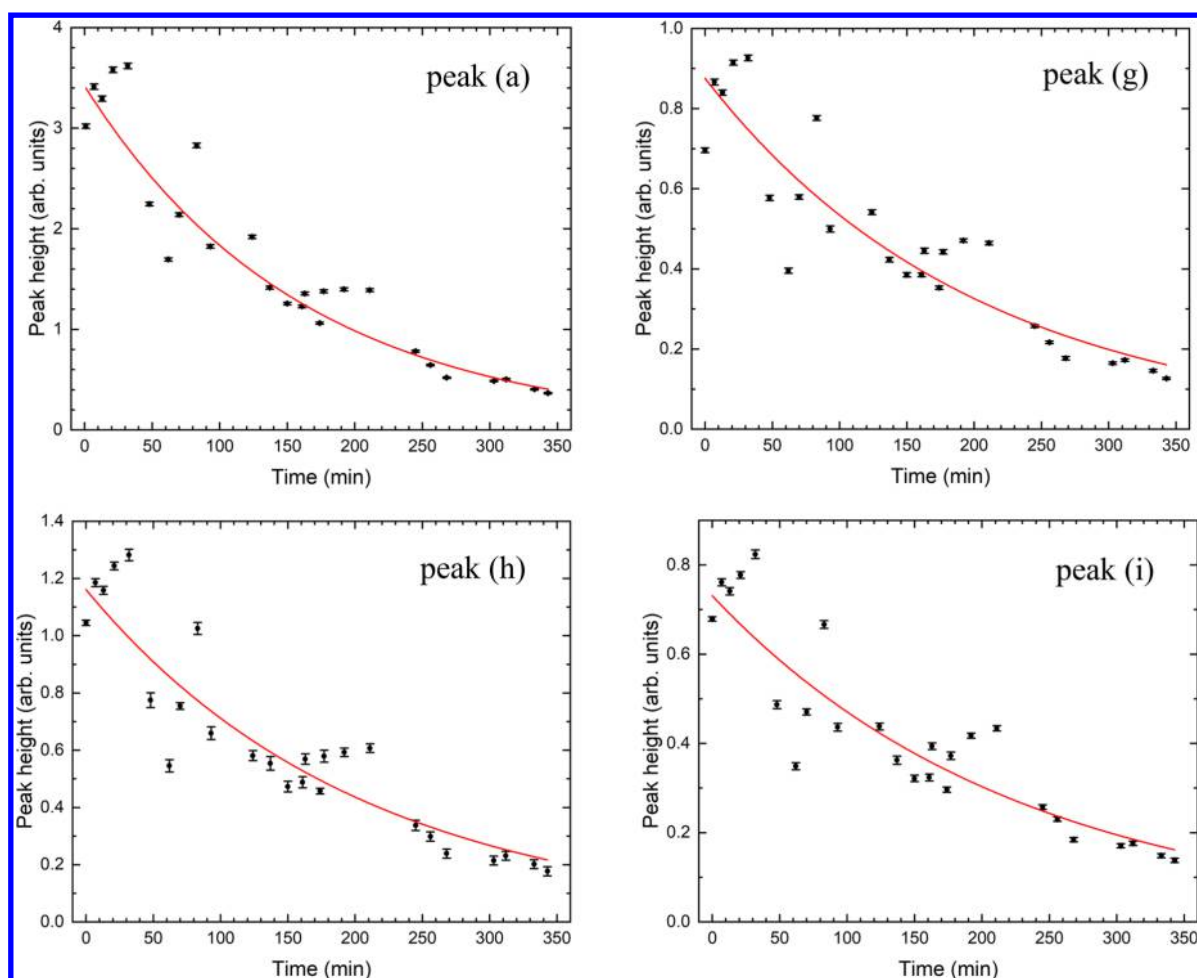


Figure 15. Fits to the decay of peaks a, g, h, and i in Figure 14 for an [MAT][DCA] droplet levitated in 0.2% NO₂ and 99.8% Ar.

For the Raman spectrum of a [BMIM][DCA] droplet levitated in 1.3% NO₂ and 98.7% Ar, the reaction caused the sharp peaks from the unreacted [BMIM][DCA] to reduce significantly and multiple broad, new features to appear. We again showed that the appearance of the new structure is consistent with the formation of organic nitro-compounds and their moieties. Adding boron nanoparticles to the unreacted [BMIM][DCA] caused the sharp peaks in the Raman spectrum to vanish and a large, structureless continuum to appear. However, after reaction with the NO₂, the new structure formed is very similar with or without the boron nanoparticles. Only a few small but significant differences could be discerned for the boron-containing sample, that is, peaks at 1440 and 732 cm⁻¹ possibly produced by the B–N stretching mode and the B–OH group of boronic acid, respectively.

In situ UV–visible reflectance spectra in the 200–1100 nm range were collected for pure and boron-doped [BMIM][DCA] droplets levitated in 1.3% NO₂ and 98.7% Ar. Owing to interaction with the NO₂ gas, the spectra developed several new reflectance minima or absorption peaks in the 200–650 nm wavelength range. The largest new structures in the UV–visible spectrum were probably formed by NO₂ and N₂O₄ dissolved in the droplet.^{52,53}

Reaction rates for the oxidation processes were studied by levitating droplets of [BMIM][DCA], boron-doped [BMIM][DCA], or [MAT][DCA] in a 0.2% NO₂ and 99.8% Ar gas

mixture. The reaction rate constants, k , were determined by analyzing the growth curves for formation of the new peaks or the decay curves for the reduction of the unreacted [BMIM][DCA] peaks in the Raman spectra as a function of time. A delay in the increase in the concentration of the product molecules was observed, which was probably a consequence of the time required for the less reacted ionic liquid in the central regions of the droplet to diffuse to the surface. For the pure [BMIM][DCA], the reaction rates for the different peaks studied range from $(1.5\text{--}2.5) \times 10^{-3} \text{ s}^{-1}$, whereas for the boron-doped [BMIM][DCA] sample the reaction rates are in the region of $(6.7\text{--}10.5) \times 10^{-4} \text{ s}^{-1}$. Thus, the nanoparticles slow the reaction rate by a factor of approximately 2.4 when averaged over all the peaks. The slower reaction rate could be caused by the increased viscosity of the droplet accompanying suspension of the small boron particles⁵⁴ rather than by chemical reactions between the boron and IL (section 3.3). For [MAT][DCA], in contrast to [BMIM][DCA], sharp new peaks formed by reaction with nitrogen dioxide were not observed, and so we could only consider the reduction in the amplitudes of peaks from the unreacted ionic liquid. The [MAT][DCA] reaction rates range from $(7.3\text{--}10.4) \times 10^{-5} \text{ s}^{-1}$ and so are a factor of approximately 20 lower than those for the pure [BMIM][DCA]. The slower reaction rate is a consequence of the [BMIM]⁺ cation differing from the [MAT]⁺ cation by carrying a butyl chain (–C₄H₉) in place of the amino functional group

($-\text{NH}_2$) and having one nitrogen atom fewer in its ring (Scheme 1). A full understanding of the different reaction rates will require calculating how the different functional groups attached to imidazolium or triazolium rings or the additional ring nitrogen atom affect the activation energies for the formation of the relevant organic nitro-compounds. For a given ionic-liquid sample, after accounting for the experimental uncertainties, the kinetic results are consistent with the anion and cation being equally degraded by the oxidation, the functional groups corresponding to the different new peaks forming at the same rate, and comparable decay and production rates.

The absence of clear evidence for the formation of new peaks in the FTIR spectra involving boron and only very minor modifications in the Raman spectrum produced by boron-containing functional groups is consistent with the [BMIM]-[DCA] capping limiting the oxidation of the nanoparticles. Further theoretical studies are required to better understand the cause of the new structure in the FTIR and Raman spectra and, hence, supplement the present empirical assignments based on functional groups. Our experimental approach thus enables the identification of the reaction intermediates and determination of the rate constants in the oxidation of ionic liquids.

AUTHOR INFORMATION

Corresponding Author

*R. I. Kaiser. E-mail: ralfk@hawaii.edu.

ORCID

Stephen J. Brotton: 0000-0002-8147-2960

Scott L. Anderson: 0000-0001-9985-8178

Ralf I. Kaiser: 0000-0002-7233-7206

Notes

The authors declare no competing financial interest.

ACKNOWLEDGMENTS

This work was supported by the Office of Naval Research under Grant N00014-16-1-2078 (Hawaii) and by the Air Force Research Laboratory in Space Propulsion (RQRS) and Propellants (RQRP) Branches at Edwards Air Force Base. Particle production was supported by the Office of Naval Research under Grant N00014-15-1-2681 (Utah).

REFERENCES

- (1) Welton, T. Room-Temperature Ionic Liquids. Solvents for Synthesis and Catalysis. *Chem. Rev.* **1999**, *99*, 2071–2083.
- (2) Endres, F.; El Abedin, S. Z. Air and Water Stable Ionic Liquids in Physical Chemistry. *Phys. Chem. Chem. Phys.* **2006**, *8*, 2101–2116.
- (3) Freemantle, M. *An Introduction to Ionic liquids*; RSC Publishing: Cambridge, U.K., 2010; p xiv, 281 pp.
- (4) Zhang, Q. H.; Shreeve, J. M. Energetic Ionic Liquids as Explosives and Propellant Fuels: A New Journey of Ionic Liquid Chemistry. *Chem. Rev.* **2014**, *114*, 10527–10574.
- (5) Brotton, S. J.; Lucas, M.; Chambreau, S. D.; Vaghjiani, G. L.; Yu, J.; Anderson, S. L.; Kaiser, R. I. Spectroscopic Investigation of the Primary Reaction Intermediates in the Oxidation of Levitated Droplets of Energetic Ionic Liquids. *J. Phys. Chem. Lett.* **2017**, *8*, 6053–6059.
- (6) Visser, A. E.; Swatloski, R. P.; Reichert, W. M.; Mayton, R.; Sheff, S.; Wierzbicki, A.; Davis, J. H.; Rogers, R. D. Task-Specific Ionic Liquids Incorporating Novel Cations for the Coordination and Extraction of Hg^{2+} and Cd^{2+} : Synthesis, Characterization, and Extraction Studies. *Environ. Sci. Technol.* **2002**, *36*, 2523–2529.

- (7) Schneider, S.; Hawkins, T.; Rosander, M.; Vaghjiani, G.; Chambreau, S.; Drake, G. Ionic Liquids as Hypergolic Fuels. *Energy Fuels* **2008**, *22*, 2871–2872.

- (8) Cardulla, F. Hydrazine. *J. Chem. Educ.* **1983**, *60*, 505–508.

- (9) Clark, J. D. *Ignition! An Informal History of Liquid Rocket Propellants*; Rutgers University Press: New Brunswick, NJ, 1972; p xiv, 214 pp.

- (10) Zhang, Y. Q.; Gao, H. X.; Joo, Y. H.; Shreeve, J. M. Ionic Liquids as Hypergolic Fuels. *Angew. Chem., Int. Ed.* **2011**, *50*, 9554–9562.

- (11) Schneider, S.; Hawkins, T.; Ahmed, Y.; Rosander, M.; Hudgens, L.; Mills, J. Green Bipropellants: Hydrogen-Rich Ionic Liquids that Are Hypergolic with Hydrogen Peroxide. *Angew. Chem., Int. Ed.* **2011**, *50*, 5886–5888.

- (12) Zhang, Y. Q.; Shreeve, J. M. Dicyanoborate-Based Ionic Liquids as Hypergolic Fluids. *Angew. Chem., Int. Ed.* **2011**, *50*, 935–937.

- (13) Xue, H.; Gao, Y.; Twamley, B.; Shreeve, J. M. New Energetic Salts Based on Nitrogen-Containing Heterocycles. *Chem. Mater.* **2005**, *17*, 191–198.

- (14) Chambreau, S. D.; Schneider, S.; Rosander, M.; Hawkins, T.; Gallegos, C. J.; Pastewait, M. F.; Vaghjiani, G. L. Fourier Transform Infrared Studies in Hypergolic Ignition of Ionic Liquids. *J. Phys. Chem. A* **2008**, *112*, 7816–7824.

- (15) Chambreau, S. D.; Koh, C. J.; Popolan-Vaida, D. M.; Gallegos, C. J.; Hooper, J. B.; Bedrov, D.; Vaghjiani, G. L.; Leone, S. R. Flow-Tube Investigations of Hypergolic Reactions of a Dicyanamide Ionic Liquid Via Tunable Vacuum Ultraviolet Aerosol Mass Spectrometry. *J. Phys. Chem. A* **2016**, *120*, 8011–8023.

- (16) McCrary, P. D.; Beasley, P. A.; Cojocaru, O. A.; Schneider, S.; Hawkins, T. W.; Perez, J. P. L.; McMahan, B. W.; Pfeil, M.; Boatz, J. A.; Anderson, S. L.; et al. Hypergolic Ionic Liquids to Mill, Suspend, and Ignite Boron Nanoparticles. *Chem. Commun.* **2012**, *48*, 4311–4313.

- (17) Cox, J. D.; Wagman, D. D.; Medvedev, V. A. *CODATA Key Values for Thermodynamics*. Hemisphere Pub. Corp.: New York, 1989; p xiii, 271 pp.

- (18) Zhou, W.; Yetter, R. A.; Dryer, F. L.; Rabitz, H.; Brown, R. C.; Kolb, C. E. Multi-Phase Model for Ignition and Combustion of Boron Particles. *Combust. Flame* **1999**, *117*, 227–243.

- (19) Young, G.; Sullivan, K.; Zachariah, M. R.; Yu, K. Combustion Characteristics of Boron Nanoparticles. *Combust. Flame* **2009**, *156*, 322–333.

- (20) Perez, J. P. L.; McMahan, B. W.; Schneider, S.; Boatz, J. A.; Hawkins, T. W.; McCrary, P. D.; Beasley, P. A.; Kelley, S. P.; Rogers, R. D.; Anderson, S. L. Exploring the Structure of Nitrogen-Rich Ionic Liquids and Their Binding to the Surface of Oxide-Free Boron Nanoparticles. *J. Phys. Chem. C* **2013**, *117*, 5693–5707.

- (21) Perez, J. P. L.; McMahan, B. W.; Yu, J.; Schneider, S.; Boatz, J. A.; Hawkins, T. W.; McCrary, P. D.; Flores, L. A.; Rogers, R. D.; Anderson, S. L. Boron Nanoparticles with High Hydrogen Loading: Mechanism for B-H Binding and Potential for Improved Combustibility and Specific Impulse. *ACS Appl. Mater. Interfaces* **2014**, *6*, 8513–8525.

- (22) Brotton, S. J.; Kaiser, R. I. Novel High-Temperature and Pressure-Compatible Ultrasonic Levitator Apparatus Coupled to Raman and Fourier Transform Infrared Spectrometers. *Rev. Sci. Instrum.* **2013**, *84*, 055114.

- (23) Brotton, S. J.; Kaiser, R. I. In Situ Raman Spectroscopic Study of Gypsum ($\text{CaSO}_4 \cdot 2\text{H}_2\text{O}$) and Epsomite ($\text{MgSO}_4 \cdot 7\text{H}_2\text{O}$) Dehydration Utilizing an Ultrasonic Levitator. *J. Phys. Chem. Lett.* **2013**, *4*, 669–673.

- (24) Xie, W. J.; Wei, B. Parametric Study of Single-Axis Acoustic Levitation. *Appl. Phys. Lett.* **2001**, *79*, 881–883.

- (25) Bennett, C. J.; Brotton, S. J.; Jones, B. M.; Misra, A. K.; Sharma, S. K.; Kaiser, R. I. High-Sensitivity Raman Spectrometer To Study Pristine and Irradiated Interstellar Ice Analogs. *Anal. Chem.* **2013**, *85*, 5659–5665.

- (26) Perez, J. P. L.; Yu, J.; Sheppard, A. J.; Chambreau, S. D.; Vaghjiani, G. L.; Anderson, S. L. Binding of Alkenes and Ionic Liquids

to B-H-Functionalized Boron Nanoparticles: Creation of Particles with Controlled Dispersibility and Minimal Surface Oxidation. *ACS Appl. Mater. Interfaces* **2015**, *7*, 9991–10003.

(27) Katsyuba, S. A.; Zvereva, E. E.; Vidis, A.; Dyson, P. J. Application of Density Functional Theory and Vibrational Spectroscopy Toward the Rational Design of Ionic Liquids. *J. Phys. Chem. A* **2007**, *111*, 352–370.

(28) Paschoal, V. H.; Faria, L. F. O.; Ribeiro, M. C. C. Vibrational Spectroscopy of Ionic Liquids. *Chem. Rev.* **2017**, *117*, 7053–7112.

(29) Kiefer, J.; Noack, K.; Penna, T. C.; Ribeiro, M. C. C.; Weber, H.; Kirchner, B. Vibrational Signatures of Anionic Cyano Groups in Imidazolium Ionic Liquids. *Vib. Spectrosc.* **2017**, *91*, 141–146.

(30) Socrates, G. *Infrared and Raman Characteristic Group Frequencies: Tables and Charts*, 3rd ed.; Wiley: Chichester, New York, 2001; p xv, 347 pp.

(31) Berg, R. W. Raman Spectroscopy and Ab-Initio Model Calculations on Ionic Liquids. *Monatsh. Chem.* **2007**, *138*, 1045–1075.

(32) Talaty, E. R.; Raja, S.; Storhaug, V. J.; Dolle, A.; Carper, W. R. Raman and Infrared Spectra and Ab Initio Calculations of C₂₋₄MIM Imidazolium Hexafluorophosphate Ionic Liquids. *J. Phys. Chem. B* **2004**, *108*, 13177–13184.

(33) Heimer, N. E.; Del Sesto, R. E.; Meng, Z. Z.; Wilkes, J. S.; Carper, W. R. Vibrational Spectra of Imidazolium Tetrafluoroborate Ionic Liquids. *J. Mol. Liq.* **2006**, *124*, 84–95.

(34) Holomb, R.; Martinelli, A.; Albinsson, I.; Lassegues, J. C.; Johansson, P.; Jacobsson, P. Ionic Liquid Structure: The Conformational Isomerism in 1-Butyl-3-Methyl-Imidazolium Tetrafluoroborate ([BMIM][BF₄]). *J. Raman Spectrosc.* **2008**, *39*, 793–805.

(35) Colthup, N. B.; Daly, L. H.; Wiberley, S. E. *Introduction to Infrared and Raman Spectroscopy*, 3rd ed.; Academic Press: Boston, 1990; p xii, 547 pp.

(36) Bibart, C.; Ewing, G. Vibrational Spectrum, Torsional Potential, and Bonding of Gaseous N₂O₄. *J. Chem. Phys.* **1974**, *61*, 1284–1292.

(37) Maier, G.; Reisenauer, H. P.; Eckwert, J.; Naumann, M.; DeMarco, M. Isomers of the Elemental Composition CN₂O. *Angew. Chem., Int. Ed. Engl.* **1997**, *36*, 1707–1709.

(38) Wu, Y. J.; Lee, Y. P. Isomers of NCO₂: IR-Absorption Spectra of ONCO in Solid Ne. *J. Chem. Phys.* **2005**, *123*, 174301.

(39) Dyke, J. M.; Jonathan, N.; Lewis, A. E.; Mills, J. D.; Morris, A. Vacuum Ultraviolet Photoelectron Spectroscopy of Transient Species. Part 16. The NCO (X²Π) Radical. *Mol. Phys.* **1983**, *50*, 77–89.

(40) Baker, J.; Butcher, V.; Dyke, J. M.; Morris, A. Vacuum Ultraviolet Photoelectron Spectroscopic Study of the NH₂O and HNO Molecules. *J. Chem. Soc., Faraday Trans.* **1990**, *86*, 3843–3851.

(41) Noble, M.; Nadler, I.; Reisler, H.; Wittig, C. The Rotationally Resolved A 1A'' ← X 1A' Spectrum of Expansion Cooled NCNO: Vibrational Fundamentals, Rotational Constants, and Perturbations. *J. Chem. Phys.* **1984**, *81*, 4333–4340.

(42) Barnes, C. E.; Brown, J. M.; Fackerell, A. D.; Sears, T. J. The Laser Magnetic Resonance Spectrum of the NCO Radical at 5.2 μm. *J. Mol. Spectrosc.* **1982**, *92*, 485–496.

(43) Thompson, W. E.; Jacox, M. E. The Infrared Spectrum of NN...CO⁺ Trapped in Solid Neon. *J. Chem. Phys.* **2011**, *135*, 224307.

(44) Nonella, M.; Muller, R. P.; Huber, J. R. Infrared Spectra, Normal Coordinate Analysis, and Photodecomposition of Matrix-Isolated NH₂NO₂, ¹⁵NH₂NO₂, ND₂NO₂, and ¹⁵ND₂NO₂. *J. Mol. Spectrosc.* **1985**, *112*, 142–152.

(45) Sheasley, W. D.; Mathews, C. W. The Ultraviolet Absorption Spectrum of HCNO in the Gas Phase. *J. Mol. Spectrosc.* **1972**, *43*, 467.

(46) Beckers, H.; Zeng, X. Q.; Willner, H. Intermediates Involved in the Oxidation of Nitrogen Monoxide: Photochemistry of the Cis-N₂O₂-O₂ Complex and of Sym-N₂O₄ in Solid Ne Matrices. *Chem. - Eur. J.* **2010**, *16*, 1506–1520.

(47) Nicolaisen, F. M.; Nielsen, O. J. Far Infrared Gas Spectra of Nitrosyl Cyanide. *J. Mol. Struct.* **1978**, *49*, 97.

(48) Parakhonskiy, G.; Dubrovinskaia, N.; Bykova, E.; Wirth, R.; Dubrovinsky, L. Experimental Pressure-Temperature Phase Diagram of Boron: Resolving the Long-Standing Enigma. *Sci. Rep.* **2011**, *1*, 96.

(49) Seoane, R. G.; Corderi, S.; Gomez, E.; Calvar, N.; Gonzalez, E. J.; Macedo, E. A.; Dominguez, A. Temperature Dependence and Structural Influence on the Thermophysical Properties of Eleven Commercial Ionic Liquids. *Ind. Eng. Chem. Res.* **2012**, *51*, 2492–2504.

(50) Kuhlmann, U.; Werheit, H.; Lundstrom, T.; Robers, W. Optical-Properties of Amorphous boron. *J. Phys. Chem. Solids* **1994**, *55*, 579–587.

(51) Werheit, H.; Schmechel, R. The Complete Optical Spectrum of Beta-Rhombohedral Boron. *J. Solid State Chem.* **1997**, *133*, 129–131.

(52) Schneider, W.; Moortgat, G. K.; Tyndall, G. S.; Burrows, J. P. Absorption Cross-Sections of NO₂ in the UV and Visible Region (200 - 700 nm) at 298 K. *J. Photochem. Photobiol., A* **1987**, *40*, 195–217.

(53) Bass, A. M.; Ledford, A. E., Jr.; Laufer, A. H. Extinction Coefficients of NO₂ and N₂O₄. *J. Res. Natl. Bur. Stand., Sect. A* **1976**, *80A*, 143.

(54) Landau, L. D.; Lifshitz, E. M. *Fluid Mechanics*, 2nd ed.; Pergamon Press: Oxford, England; New York, 1987; p xiii, 539 pp.